

Impact cratering mechanics: A forward approach to predicting ejecta velocity distribution and transient crater radii

Kosuke Kurosawa ^{1a}, Satoshi Takada^b

^a*Planetary Exploration Research Center, Chiba Institute of Technology, 2-17-1, Narashino, Tsudanuma, Chiba 275-0016, Japan*

^b*Earthquake Research Institute, The University of Tokyo, 1-1-1, Yayoi, Bunkyo-ku, Tokyo 113-0032, Japan*

Abstract

Impact craters are among the most prominent topographic features on planetary bodies. Crater scaling laws allow us to extract information about the impact histories on the host bodies. The π -group scaling laws (e.g., Holsapple and Schmidt, 1982) have been constructed based on the point-source approximation, dimensional analysis, and the results from laboratory and numerical impact experiments. Recent laboratory and numerical impact experiments, however, demonstrated that the scaling parameters themselves exhibit complex behavior against the change in the impact conditions and target properties. Since impact experiments are expensive and time-consuming in terms of obtaining new scaling constants, it is not feasible to explore the entire parameter space via experiments. Here, we propose

¹Corresponding author

Kosuke Kurosawa, Ph.D.

Planetary Exploration Research Center, Chiba Institute of Technology

E-mail: kosuke.kurosawa@perc.it-chiba.ac.jp

Tel: +81-47-4782-0320

Fax: +81-47-4782-0372

an alternative, fully analytical method to predict impact outcomes, including the ejection velocity distribution and transient crater radii, based on impact cratering mechanics. This approach is based on the Maxwell Z -model [Maxwell, 1977, *Impact and Explosion Cratering*, New York: Pergamon Press, pp. 1003–1008] and the residual velocity [Melosh, 1985, *Icarus* **62**, 339–343]. Given that the shapes of the streamlines of the excavation flow and the kinetic energy in a given streamtube are known, we can calculate the ejecta velocity distribution and investigate the cessation of crater growth. We present analytical expressions of (1) the proportionality relation between the ejection velocity and the ejection position, (2) the radius of a growing crater as a function of time, and (3) the transient crater radii in the gravity- and strength-dominated regimes. Since we focused on obtaining analytical solutions in this study, a number of simplifications are employed, such as a priori assumption of the direction of the velocity vectors of the excavating materials, the neglect of the effects of dry friction, metal-like targets with a constant yield strength. Due to the simplifications in the strength model, the accuracy of the prediction in the strength-dominated cratering regime is relatively low. Our model reproduces the power-law behavior of the ejecta velocity distribution and the approximate time variation of a growing crater predicted by π -group scaling laws. In our model, the transient crater radius depends strongly on the shape exponent Z , the shock decay exponent n , and the exponent m pertaining to the residual velocity. Thus, the nature of shock propagation and the thermodynamic response of the shocked media, which cannot be addressed by dimensional analyses as a matter of principle, are naturally included in our estimation. The predicted radii under typi-

cal impact conditions mostly converge to a region between the two typical scaling lines for dry and wet sands predicted by the π -group scaling laws, strongly supporting the notion that the new method is one of the simplest ways to predict impact outcomes, as it provides analytical solutions. Our model could serve as a quick-look tool to estimate the impact outcome under a given set of conditions, and it might provide new insights into the nature of impact excavation processes. (463 words)

Keywords: Impact cratering mechanics, Shock propagation, Crater size, Ejection velocity, Scaling laws

1. Introduction

Impact craters are among the dominant geographical features on planets, satellites, and small bodies without a hydrosphere or atmosphere. Craters provide evidence that the host body has suffered intense impact bombardment throughout its history (e.g., Neukum and Ivanov, 1994, Ryder, 2002, Robbins, 2014, Fassett, 2016). The crater size and ejecta deposits around the host crater, as observed using remote sensing methods, could constrain the impact history on a given planetary body. Thus, the relationship between impact conditions and impact outcomes has been investigated extensively using both experimental and numerical methods. The widely used π -group scaling laws have been constructed using such information about crater formation (e.g., Holsapple and Schmidt, 1982, Schmidt and Housen, 1987, Holsapple, 1993, Johnson et al., 2016, Prieur et al., 2017).

The π -group scaling laws have been constructed based on the ‘point-source theory’ and dimensional analysis (e.g., Buckingham, 1914, Dienes and Walsh,

1970, Holsapple and Schmidt, 1982, 1987). First, we briefly discuss the point-source theory. It is widely believed that impact-related processes during the late stages of impact phenomena, including the crater radius and the ejecta velocity distribution, can be described by a single quantity, the coupling parameter C (e.g., Dienes and Walsh, 1970, Holsapple and Schmidt, 1982, Holsapple, 1993), as follows:

$$C = R_p v_{\text{imp}}^\mu \rho_p^\nu, \quad (1)$$

where R_p , v_{imp} , μ , ρ_p , and ν are the projectile radius, the impact velocity, a velocity-scaling exponent, the projectile density, and a density-scaling exponent, respectively. The presence of coupling parameter was originally reported as “the late-stage equivalence” based on a series of numerical experiments, which modeled collisions between two identical metals (Dienes and Walsh, 1970). Subsequently, the term ρ_p^ν was introduced to address a density contrast between the projectile and the target (e.g., Holsapple and Schmidt, 1982). The velocity-scaling exponent μ was estimated at 0.58 ± 0.01 for consolidated materials (Dienes and Walsh, 1970). This value is applicable for impact velocities well above the target sound speed. The exponent μ can range from $1/3$ (momentum scaling) to $2/3$ (energy scaling) under the different impact conditions (e.g., Dienes and Walsh, 1970). Mizutani et al. (1983, 1990) have pointed out that the late-stage equivalence holds only for an intermediate range of shock pressure and that μ is related to the pressure decay exponent in the pressure range. In the late-stage equivalence, the point-source approximation is the most important assumption.

Second, we describe the concept of the dimensional analysis. Using seven variables related to the diameter of a transient crater D_{tr} , the impact velocity

v_{imp} , the projectile diameter D_p , gravitational acceleration g , the strength of the target body Y , projectile density ρ_p , and target density ρ_t , four independent dimensionless parameters (π_D , π_2, π_3 , and π_4) can be derived:

$$\pi_D = D_{\text{tr}} \left(\frac{\rho_t}{M_p} \right)^{\frac{1}{3}}, \quad (2)$$

$$\pi_2 = \left(\frac{4\pi}{3} \right)^{\frac{1}{3}} \frac{g D_p}{v_{\text{imp}}^2} = \frac{1}{16} \left(\frac{4\pi}{3} \right)^{\frac{4}{3}} \frac{\rho_p g D_p^4}{E_{\text{proj}}}, \quad (3)$$

$$\pi_3 = \frac{Y}{\rho_t v_{\text{imp}}^2}, \quad (4)$$

$$\pi_4 = \frac{\rho_t}{\rho_p}, \quad (5)$$

where $M_p = (\pi/6)\rho_p D_p^3$ and $E_{\text{proj}} = M_p v_{\text{imp}}^2/2$ are the projectile mass and the initial kinetic energy of the impactor, respectively. The four parameters π_D , π_2, π_3 , and π_4 are often referred to as the scaled crater diameter, the gravity-scaled size, the non-dimensional strength, and the density ratio, respectively. Detailed descriptions of all dimensionless variables can be found in the literature (e.g., Melosh, 1989). By combining these parameters with the coupling parameter, the functional relationship between a dimensionless measure of the crater diameter π_D and the other variables is obtained as follows (Holsapple, 1993):

$$\pi_D = K_1 \left[\pi_2 \pi_4^{-\frac{\mu+2-6\nu}{3\mu}} + \left(\pi_3 \pi_4^{-\frac{2-6\nu}{3\mu}} \right)^{\frac{\mu+2}{2}} \right]^{\frac{-\mu}{\mu+2}}, \quad (6)$$

where K_1 is a scaling constant. Note that Eq. (6) is a full description, which covers both the gravity-dominated ($\pi_2 \gg \pi_3$) and strength-dominated ($\pi_2 \gg \pi_3$) regimes. A similar formulation pertaining to the ejecta velocity distribution has been proposed (e.g., Housen et al., 1983, Housen and Holsapple,

2011). It should be mentioned that, in principle, dimensional analysis does not provide absolute values, including the position-dependent ejection velocity and the transient crater radius. Thus, the scaling parameters, including K_1 , μ , and ν , have been widely explored empirically based on both laboratory and numerical experiments (e.g., Gault, 1973, Gault and Wedekind, 1977, Schmidt, 1980, Schmidt and Housen, 1987, O’Keefe and Ahrens, 1993, Cintala et al., 1999, Wünnemann et al., 2006, 2011, 2016, Yamamoto et al., 2006, Baldwin et al., 2007, Elbeshausen et al., 2009, Kraus et al., 2011, Kenkmann et al., 2011, Suzuki et al., 2012, Güldemeister, 2015, Prieur et al., 2017). However, existing data pertaining to crater radii have not converged to the single universal line predicted by Eq. (6) (e.g., Melosh, 1989). In addition, recent laboratory/numerical impact experiments show that the scaling parameters themselves exhibits a complex behavior against the change in the impact/target conditions, such as impact velocity v_{imp} (Barnouin-Jha et al., 2007, Yamamoto et al., 2017), internal friction f and porosity ϕ (e.g., Wünnemann et al., 2006, Elbeshausen et al., 2009, Prieur et al., 2017).

The complexity of the scaling laws, as discussed in the previous paragraph, might originate from the limitations pertaining to dimensional analysis, which in principle cannot describe the mechanical aspects of impact cratering processes. In addition, both laboratory and numerical experiments are highly time-consuming and expensive in terms of exploring the entire parameter space. Thus, the objective of this study is to develop the first fully analytic method to estimate crater size and the ejection velocity distribution, without reliance on the π -group scaling laws. Although the model requires several assumptions or simplifications, as discussed below, it can provide the

full chain of relations connecting the projectile/target parameters with the impact outcomes, including the ejecta velocity distribution and the transient crater radii. Since the fully analytic model allows us to quickly examine the parameter dependence on the impact outcomes, it would greatly help to minimize the required number of shots in future laboratory and numerical experiments to obtain new, high-accuracy scaling parameters. Here, we briefly describe the steps included in the model, as follows: (1) estimate at each target point the peak particle velocity at the shock front, (2) remap the peak-particle velocity to the prescribed incompressible flow field, (3) evaluate the kinetic energy in each streamtube, (4) calculate the residual kinetic energy at the moment when the materials in a streamtube will lift above the pre-impact target surface, and (5) find the streamtube where the initial kinetic energy would be completely spent on work as a function of gravity and strength energy. Step (4) allows us to estimate the ejecta velocity at the distance where the streamtube leaves the target, and step (5) allows us to determine the transient cavity radius.

Two key models are used in steps (2) and (3): the concept of the residual velocity and Maxwell’s Z -model, respectively. The former was proposed by Melosh (1985), who derived a relationship between shock propagation and the subsequent excavation flow based on thermodynamics. Although the behavior of shock propagation has been studied extensively (e.g., Perret and Bass, 1975), the link between the initial compressible radial flow and a late-stage incompressible excavation flow was unknown at the time. Melosh (1985) pointed out that the residual velocity $u_{p,res}$, which corresponds to the particle velocity upon the arrival of a subsequent expansion wave, is the origin

of the normal excavation flow. During a shock-release cycle, the absolute magnitude of the particle velocity is significantly reduced owing to the expansion toward the free surface, and the direction of the velocity vectors of the shocked materials is changed significantly from that of the downward-propagating shock wave. The shocked materials with residual velocities form an excavation flow directed upward. The magnitude of the residual velocity can be estimated from thermodynamics by employing an equation of state (EOS) and the integral of the Riemann invariant along the isentrope from the shocked to the reference state. The latter analytic model was constructed by Maxwell (1977) to predict the geometry of the late-stage incompressible flow. A combination of the residual velocity and the streamlines calculated based on the Z -model allows us to accomplish steps (2) and (3).

2. Rationale

In this section, we describe the basic principles of our model. The Maxwell Z -model is briefly described in Section 2.1, and the procedure used to calculate the residual velocity following a shock-release cycle from the peak-particle-velocity distribution is described in Section 2.2. Finally, in Section 2.3 we discuss how to calculate crater radii and the ejecta velocity distribution under a given impact condition.

2.1. Shapes of the streamlines of the excavation flow

We use the Z -model to construct the geometry of the excavation flow. The radial velocity u_r below the pre-impact surface is as follows (Maxwell, 1977):

$$u_r = \alpha(t)r^{-Z}, \quad (7)$$

where $\alpha(t)$, r , and Z are the time-dependent strength of the excavation flow, the distance from the impact point, and a decay exponent that determines the curvature of the flow field, respectively. If the excavation flow is incompressible, the angular component of the flow velocity u_θ in polar coordinates (r, θ) can be calculated using the incompressibility constraint $\nabla \cdot \mathbf{u} = 0$. The geometry of the streamlines is given by

$$r = R(1 - \cos \theta)^{\frac{1}{Z-2}}, \quad (8)$$

where R is the horizontal distance from the impact point to the intersection of a given streamline and the pre-impact surface. The $\theta = 0$ axis is directed vertically downward. Figure 1 shows examples of the shapes of streamlines considered here. To describe the impact excavation, Z must exceed two. If $Z = 2$, the excavation flow becomes a purely radial flow, and it never reaches the surface for $Z \leq 2$. Note that $\alpha(t)$ is not needed to describe the shapes of the streamlines and that the explicit form of $\alpha(t)$ is not given by the Z -model on its own. Thus, one of the simplest assumptions (i.e., that $\alpha(t)$ is time-independent) has been used frequently (e.g., Housen et al., 1983). In other words, such previous studies used the Z -model only to describe the streamlines in a steady state. The cessation of crater growth, however, cannot be addressed by assuming $\alpha(t) = \text{Const}$.

In this study, we only discuss crater growth in the horizontal direction. Here, we briefly discuss the difficulties in estimating the vertical growth, as follows. The original version of the Maxwell Z -model predicts that the shape of the growing cavity should be a hemisphere, because the radial component of the particle velocity u_r exhibits a one-dimensional form as a function of distance, r (Eq. (7)). In contrast, it is known that the actual crater growth

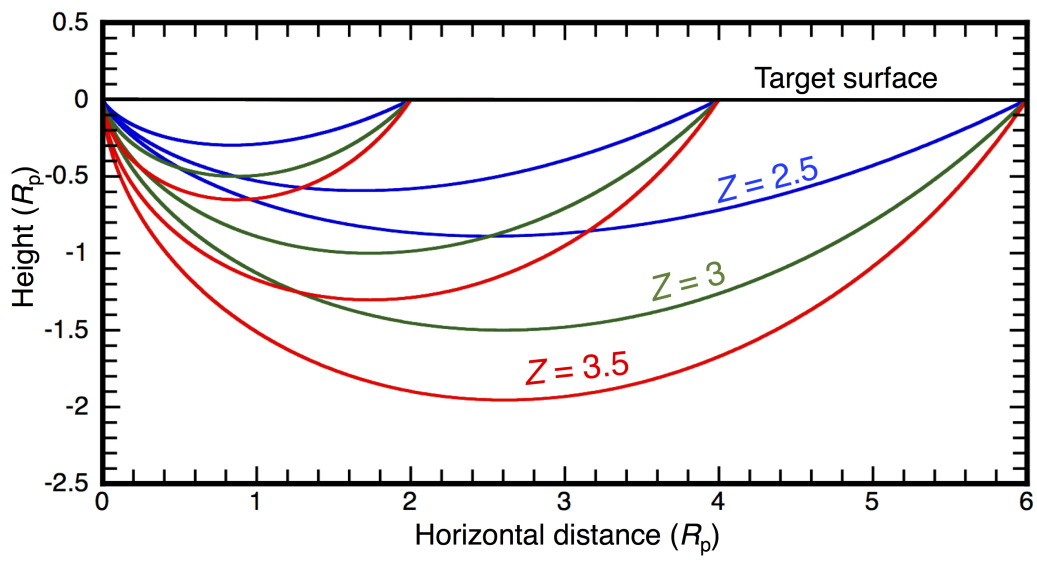


Figure 1: Examples of the shapes of streamlines predicted by the Maxwell Z -model. We used $Z = 2.5$ (blue), 3.0 (green), and 3.5 (red). The x and y axes are normalized by the projectile radius, R_p .

on most geologic materials, like sand and fragmented rocks, is characterized by two stages, as follows. Hemispheric cavity growth stops when its maximum depth is reached, and crater growth in the horizontal direction ceases on timescales that are several times longer (Barnouin-Jha et al., 2007, Yamamoto et al., 2009, 2017). Hence, we divide the streamlines predicted by the Z -model into “excavation” and “displacement” components. The former corresponds to streamlines within the transient crater radius; i.e., the material covered by this component is ejected from the pre-impact target surface. The material associated with the latter component is never launched from the surface, although this part contributes to structural uplift during the final phase of crater formation. Thus, the former and latter components contribute mainly to crater growth in the horizontal and vertical directions, respectively. Figure 2 shows a schematic diagram of the components’ Z -trajectories. In realistic cases, the earlier cessation of crater growth in the vertical direction is, as mentioned above, expected to result from resistance to displacement owing to dynamic rebound, which comes from the pressure gradient produced by the isostatic pressure, and the depth-dependent strength caused by dry friction in the geologic media through isostatic pressure. Thus, the actual crater growth will deviate from the hemispherical cavity growth predicted by the Z -model. Such dynamic effects cannot be treated based on an analytical approach without the functional form of the time-dependent flow strength, $\alpha(t)$. In contrast, the streamlines in the excavation component, which mainly contribute to growth in the horizontal direction, can be approximated by the Z -model, as they are not strongly affected by depth-dependent effects. Note that this treatment is unphysical in a strict sense, because a huge strain is

produced between both components along the boundary.

There is another reason why we do not address the crater depth in this study. In reality, the central point of the excavation flow is located somewhat below the pre-impact surface (e.g., Croft, 1980). Nevertheless, we decided to neglect this burial depth in the following discussion, as the effect of burial depth on crater radius is relatively small, although it significantly affects the crater depth (e.g., Croft, 1980, Stewart and Valiant, 2006, Kurosawa, 2015). This simplification allows us to easily solve the system of equations analytically. Figure 1 shows examples of the shapes of streamlines considered here. To describe the impact excavation, Z must exceed two. If $Z = 2$, the excavation flow becomes a purely radial flow, and it never reaches the surface for $Z < 2$.

2.2. Residual velocity following a shock-release sequence

Here, we describe the key concept of our model, based on the discussion by Melosh (1985), which is that the excavation flow is driven by the residual velocity following a shock-release cycle. The peak-particle velocity distribution in geological media has been investigated by means of large-scale nuclear explosions. In this study, we used the data compilation of Perret and Bass (1975). The peak-particle velocity distribution, $u_{p,\max}(r)$, as a function of distance from the impact point r , is as follows (e.g., Croft, 1982):

$$u_{p,\max}(r) = u_{p0} \quad (r < R_p); \quad (9)$$

$$u_{p,\max}(r) = u_{p0} \left(\frac{r}{R_p} \right)^{-n} \quad (r > R_p), \quad (10)$$

where $u_{p,\max}$, r , u_{p0} , R_p , and n are the peak particle velocity at a given position, the distance from the impact point, the peak-particle velocity in an

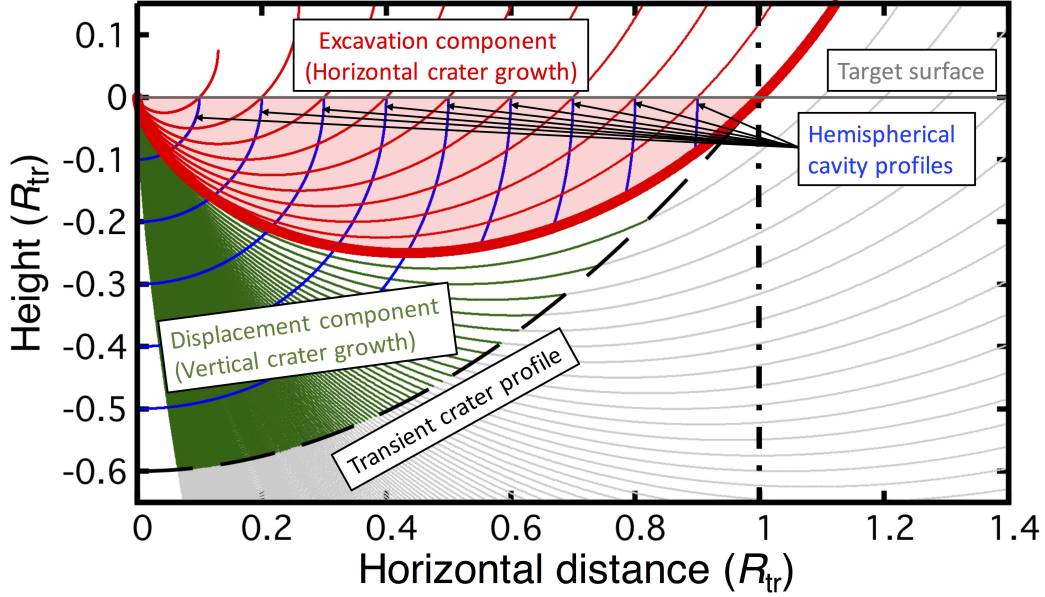


Figure 2: Schematic diagram of the excavation and displacement components of the flow field in the Z -model (see Section 2.1). The horizontal and vertical axes are normalized by the transient crater radius R_{tr} . The red curves are for the excavation component. The red shaded region has been excavated from the target. The blue curves indicate the hemispherical transient-cavity profiles originally predicted by the Z -model. The thick black dashed curve represents the actual cavity profile of a transient crater. The green curves correspond to the flow in the displacement component. We assumed that the hemispherical cavity growth proceeds approximately until $R_{cr} = 0.5R_{tr}$, where R_{cr} is the radius of a growing crater. At some later time, the target's displaced volume reaches a maximum owing to depth-dependent effects (see Section 2.1), while the materials in the excavation component continue to move, having been ejected above the target surface.

isobaric core, the projectile radius, and the shock decay exponent, respectively. For alluvium, tuff, and granite, a shock decay exponent of $n = 1.87$ has been reported for $u_{p,\max}$ between 0.03 and 5 km s⁻¹ (Perret and Bass, 1975, Melosh, 1984, 1989). Since $n = 1.87$ is valid for both igneous and sedimentary rocks, Melosh (1984) used the value as a universal value. Hence, we employed this value as throughout this manuscript by following Melosh (1984). The one-dimensional impedance matching solution has been widely used to estimate u_{p0} under a given impact condition (e.g., Melosh, 1989). If we consider a collision between two identical bodies, u_{p0} becomes half of v_{imp} . Although u_{p0} depends on shock Hugoniot parameters, including the reference density ρ_0 , the bulk sound speed C_0 , and a constant s pertaining to collisions between two different materials, u_{p0} is linearly proportional to v_{imp} . The peak-particle-velocity distribution, Eq. (10), is rather similar to the radial component of the particle velocity in the Z -model; see Eq. (7). This peak-particle-velocity distribution, however, does not predict any excavation flow, because the exponent n is less than 2.

After the shock wave's passage, a rarefaction wave propagates into the compressed materials from the free surface. The compressed materials expand toward the free surface following the arrival of the rarefaction wave. This expansion is broadly approximated as an adiabatic process; i.e., $dS = 0$, where S is the entropy. The adiabatic expansion is physically the same as the propagation of an expansion wave from the free surface. The propagating direction of the expansion wave is similar to that of the shock wave far from the impact point (e.g., Melosh, 1985, Kurosawa et al., 2018). Since the compressed materials are accelerated into the opposite direction of the

propagating expansion wave, the pressure release causes a deceleration of the compressed materials from $u_{\text{p,max}}$ to $u_{\text{p,res}}$, where $u_{\text{p,res}}$ is the residual velocity after the pressure release. The magnitude of change in the particle velocity during adiabatic expansion Δu_{p} can be calculated by integrating the Riemann invariant along the isentrope (Melosh, 1985):

$$\Delta u_{\text{p}} = \int_{\rho_{\text{H}}}^{\rho_0} \frac{C_{\text{R}}}{\rho} d\rho \quad (11)$$

$$C_{\text{R}} = \sqrt{\left. \frac{\partial P}{\partial \rho} \right|_S} \quad (12)$$

where ρ_0 , ρ_{H} , ρ , P , and C_{R} are the reference density, the density in the peak shock state, the density during expansion, the pressure during expansion, and the sound speed in the compressed matter, respectively. The decreases in pressure and density during isentropic release are constrained by the first and second laws of thermodynamics; i.e.,

$$dE = \frac{P(E, \rho)}{\rho^2} d\rho, \quad (13)$$

where E is the internal energy during expansion. The pressure $P(E, \rho)$ in Eq. (13) is given by the EOS. In this study, the Tillotson EOS (Tillotson, 1962) was used to integrate Eq. (11) by combination with Eqs. (12) and (13). The pressure, as a function of both internal energy E and density ρ is given by

$$P = P_{\text{thermal}}(E, \rho) + P_{\text{cold}}(\rho), \quad (14)$$

where P_{thermal} and P_{cold} are the thermal and cold pressures, respectively. The explicit expressions of P_{thermal} and P_{cold} are included in Appendix A. The velocity change Δu_{p} is slightly smaller than $u_{\text{p,max}}$ because of the entropy

increase due to the irreversible shock heating (Melosh, 1985). If we assume that the propagating directions of both the shock and expansion waves are the same, which is a reasonable assumption far from the impact point, the magnitude of the residual velocity after a shock-release cycle $u_{p,\text{res}}$ is given by

$$u_{p,\text{res}} = u_{p,\text{max}} - \Delta u_p. \quad (15)$$

The direction of $u_{p,\text{res}}$ is mostly different from that of $u_{p,\text{max}}$ because of the subtly different propagating directions of the shock and expansion waves (e.g., Melosh, 1989). Here, we introduce a key assumption to solve the system of equations, which is that the materials following a shock-release cycle are injected into an excavation flow along a streamline at velocity $u_{p,\text{res}}$, as shown in Figure 3. Figure 3a is a schematic diagram of the cratering flow field assumed in our model. We assumed that the shock-driven material movement during a shock-release cycle, which occurs typically within $1 t_s$ (where $t_s = D_p/v_{\text{imp}}$ is the characteristic timescale for projectile penetration), can be neglected. In other words, the shocked materials attain a particle velocity $u_{p,\text{res}}$ after pressure release from their initial positions. These assumptions allow us to analytically estimate the kinetic energy available to drive material ejection in a given streamtube, as discussed in the next section. The spatial distributions of the pressure and density in the initial-peak-shock state after a single impact event, which provide the initial conditions for the integration of Eq. (11), are calculated based on the Rankine-Hugoniot relations and Eqs. (9) and (10) for a given impact condition.

Here, we note about the difference between impact spallation and normal excavation. The resultant particle velocity after a shock-release cycle strongly

depends on the geometric configuration, especially on the angle between the propagation directions of the shock and expansion waves (Kurosawa et al., 2018). For materials initially located near the free surface, Eq. (15) does not hold, because the angle between two waves becomes $\sim 90^\circ$, resulting in high-speed ejecta caused by impact spallation (Kurosawa et al., 2018). Since the mass ejected by spallation is estimated to be much smaller than that from normal excavation considered in this study (e.g., Melosh, 1984, Kurosawa et al., 2018), we neglected the near-surface wave interactions.

2.3. Impact ejection and cessation of crater growth

Given that the shapes of the streamlines and the kinetic energy in a streamtube have been obtained, we can now assess the energy balance of the kinetic, gravitational, and strength energies (E_{kin} , E_{grav} , and E_{strength} , respectively) at a given horizontal distance R . The strength energy is the energy required to move materials supported by a yield strength Y . The mass of a streamtube M_{tube} between $R - \Delta R$ and R is calculated using the following volume integral in polar coordinates:

$$M_{\text{tube}}(R) = 2\pi\rho_t \int_{R-\Delta R}^R \int_0^{\frac{\pi}{2}} r^2 \sin\theta dr d\theta, \quad (16)$$

where ΔR and ρ_t are a small increment in the horizontal distance and the reference density of the target, respectively. E_{kin} , E_{grav} , and E_{strength} are expressed as

$$E_{\text{kin}}(R) = 2\pi\rho_t \int_{R-\Delta R}^R \int_0^{\frac{\pi}{2}} \frac{u_{\text{p,res}}^2}{2} r^2 \sin\theta dr d\theta, \quad (17)$$

$$E_{\text{grav}}(R) = 2\pi\rho_t \int_{R-\Delta R}^R \int_0^{\frac{\pi}{2}} g z r^2 \sin\theta dr d\theta, \quad (18)$$

and

$$E_{\text{strength}}(R) = 2\pi \int_{R-\Delta R}^R \int_0^{\frac{\pi}{2}} \varepsilon Y r^2 \sin \theta dr d\theta, \quad (19)$$

where $z = r \cos \theta$ is the height from the pre-impact surface and ε is the volumetric strain. If E_{kin} is greater than the sum of E_{grav} and E_{strength} at a given distance R , the materials in the streamtube are ejected. The ejection velocity v_{ej} is estimated from energy conservation as

$$v_{\text{ej}} = \sqrt{\frac{2(E_{\text{kin}} - E_{\text{grav}} - E_{\text{strength}})}{M_{\text{tube}}}}. \quad (20)$$

Given that the characteristic velocity of the material in each streamtube v_{ch} is roughly approximated by $v_{\text{ch}} \sim v_{\text{ej}}$, the time variation in the radius of a growing crater $R_{\text{cr}}(t)$ can be obtained as a first-order estimate. The time t_{ej} when ejection occurs, from position R , is estimated as

$$t_{\text{ej}} = \frac{L}{v_{\text{ch}}}, \quad (21)$$

where L is the total travel distance along the streamline, and $L = f(Z)R$, where $f(Z)$ is a constant that depends only on Z . The exact form of $f(Z)$ is presented in Appendix B. The time variation of $R_{\text{cr}}(t)$ is given by

$$R_{\text{cr}}(t) = \frac{v_{\text{ch}}}{f(Z)} t_{\text{ej}}. \quad (22)$$

Cessation of the growth of a crater occurs when $E_{\text{kin}} = E_{\text{grav}}$ or $E_{\text{kin}} = E_{\text{strength}}$ in the gravity- or strength-dominated regimes, respectively. These conditions provide an absolute value of the transient crater radius R_{tr} under a given impact condition.

Most of the equations described in this section can be solved analytically if the shock decay exponent n , the Tillotson and shock Hugoniot parameters,

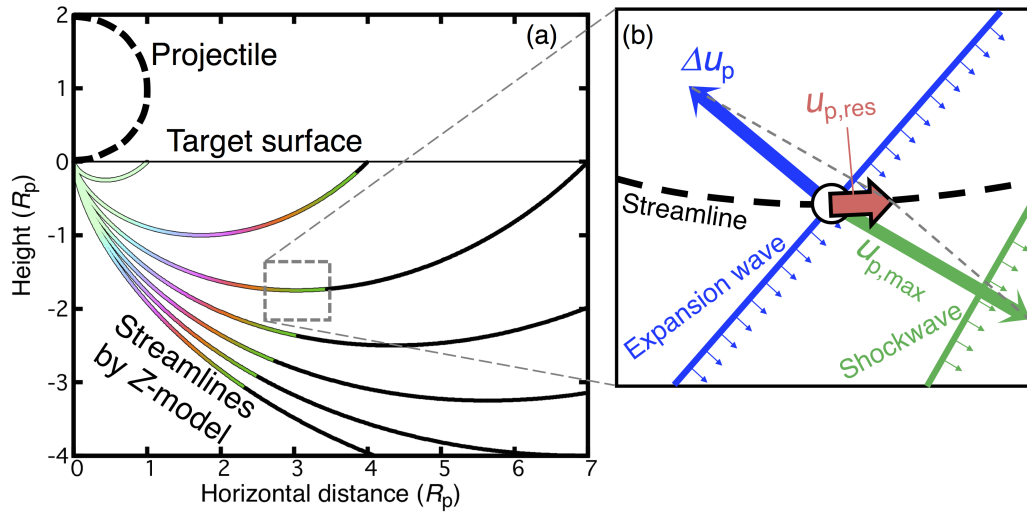


Figure 3: Schematic diagram of the situation considered in the proposed model. (a) The streamlines are schematically highlighted in color depending of the residual velocity. Black color indicates that the residual velocity is zero; i.e., subsonic conditions, where the compressional wave speed U is slower than the longitudinal sound speed C_L (See Section 3.1). (b) Close-up of the area indicated by the rectangle in (a). The directions and magnitudes of the velocity vectors $u_{p,max}$, Δu_p , and $u_{p,res}$ are shown schematically in panel (b). The directions of the propagating shock and expansion waves are also shown.

and the basic quantities v_{imp} , D_p , g , Y , ρ_p , and ρ_t are known. The exceptions can also be integrated easily using a spreadsheet. Consequently, our model can be used to estimate the absolute value of R_{tr} analytically without reliance on the π -group scaling laws.

It should be mentioned that O’Keefe and Ahrens (1981), Ivanov (1983), and Richardson et al. (2007) proposed similar analytical models, although with key differences to the present model. O’Keefe and Ahrens (1981) addressed the controls on transient crater depth, not the crater diameter, and did not include the effects of the residual velocity in their model. Ivanov (1983) also employed the geometry predicted by the Z -model to calculate mechanical plastic work in ideal plastic media with a constant yield strength. He estimated the decay of the ejection velocity with respect to the horizontal distance from the impact point in the strength-dominated regime. The model proposed by Richardson et al. (2007) was constructed by means of a combination of Maxwell’s Z -model and point-source theory to systematically investigate the effects of gravitational acceleration, target density, and target strength on ejection behavior in the framework of the π -group scaling laws.

3. Results

In this section, we present explicit expressions for the variables described in Section 2 as well as the results of our calculations. First, we discuss the residual velocity $u_{\text{p,res}}$ as a function of the peak particle velocity behind the shock wave $u_{\text{p,max}}$ (Section 3.1). Second, in Section 3.2 we show the integrated results of the energies in a streamtube. Third, the ejection behavior, including the time evolution of the radius of a growing crater and the ejection

tion velocity distribution, is described in Section 3.3. Finally, we present the resultant crater sizes R_{tr} in Section 3.4.

3.1. Residual velocity

We calculated the residual velocity $u_{\text{p,res}}$ using Eqs. (9)–(15). Figure 4 shows $u_{\text{p,res}}$ as a function of $u_{\text{p,max}}$ for granite. We found that $u_{\text{p,res}}$ is approximated by two power-law functions with coefficients C (C_c and C_t) and exponents m (m_c and m_t), as follows:

$$u_{\text{p,res}}(r) = C u_{\text{p,max}}(r)^m, \quad (23)$$

where

$$C = C_t \text{ and } m = m_t \quad (u_{\text{p,max}}(r) > u_{\text{p,sw}}), \quad (24)$$

$$C = C_c \text{ and } m = m_c \quad (u_{\text{p,th}} < u_{\text{p,max}}(r) < u_{\text{p,sw}}), \quad (25)$$

where $u_{\text{p,sw}}$ and $u_{\text{p,th}}$ are switching and threshold velocities, respectively. Note that the subscripts “t” and “c” mean ‘thermal’ and ‘cold,’ respectively. The switching velocity corresponds to the transition from the cold-pressure-dominated regime ($P_{\text{cold}} > P_{\text{thermal}}$) to its thermal-pressure-dominated counterpart ($P_{\text{cold}} < P_{\text{thermal}}$) with increasing $u_{\text{p,max}}$. The threshold velocity corresponds to the transition from the elastic-plastic state to the shocked state in a diagram showing the wave speed U versus the particle velocity u_{p} . The definition of $u_{\text{p,th}}$ is provided in Appendix C. The absolute magnitude of the residual velocity is estimated to range from 4% to 20% of that of the peak particle velocity. A higher $u_{\text{p,max}}$ leads to a higher $u_{\text{p,res}}$ because the shock-induced entropy is enhanced at higher shock pressures. Figure 5 is the same

as Figure 4, except that the former shows the $u_{p,\text{res}} - u_{p,\text{max}}$ relation pertaining to various materials. The Tillotson parameters used in the calculations were taken from Melosh (1989) and Benz and Asphaug (1999). These results suggest that the combination of two power laws leads to a unified equation to describe the behavior of $u_{p,\text{res}}$ with increasing $u_{p,\text{max}}$. The best-fitting values for C and m are listed in Table 3.1. We checked the absolute magnitude of the residual velocity based on a comparison with a hydrocode. The limitations of our model are described in Section 4.1.

Table 1: Parameters relating to the residual velocity

	Granite	Basalt	Water	Aluminum	Iron
$u_{p,\text{th}}^1$ (km/s)	0.804	0.730	1.48 ²	0.887	0.652
$u_{p,\text{sw}}$ (km/s)	2.12	2.67	5.03	5.45	3.19
C_c	0.0412	0.0281	0.0796	0.0187	0.0235
m_c	1.97	2.29	1.39	2.00	2.14
nm_c^3	3.69	4.28	2.60	3.73	4.00
C_t	0.0833	0.0827	0.145	0.0655	0.0691
m_t	1.20	1.21	1.04	1.26	1.25
nm_t	2.25	2.27	1.95	2.36	2.34

¹The parameters C_0 and s are taken from Melosh (1989). The longitudinal sound speeds C_L are calculated using the Poisson ratio and C_0 .

²Since liquid water is considered here, C_L corresponds to the bulk sound speed C_0 .

³The decay exponent n is assumed to be constant, $n = 1.87$ (see Section 2.2).

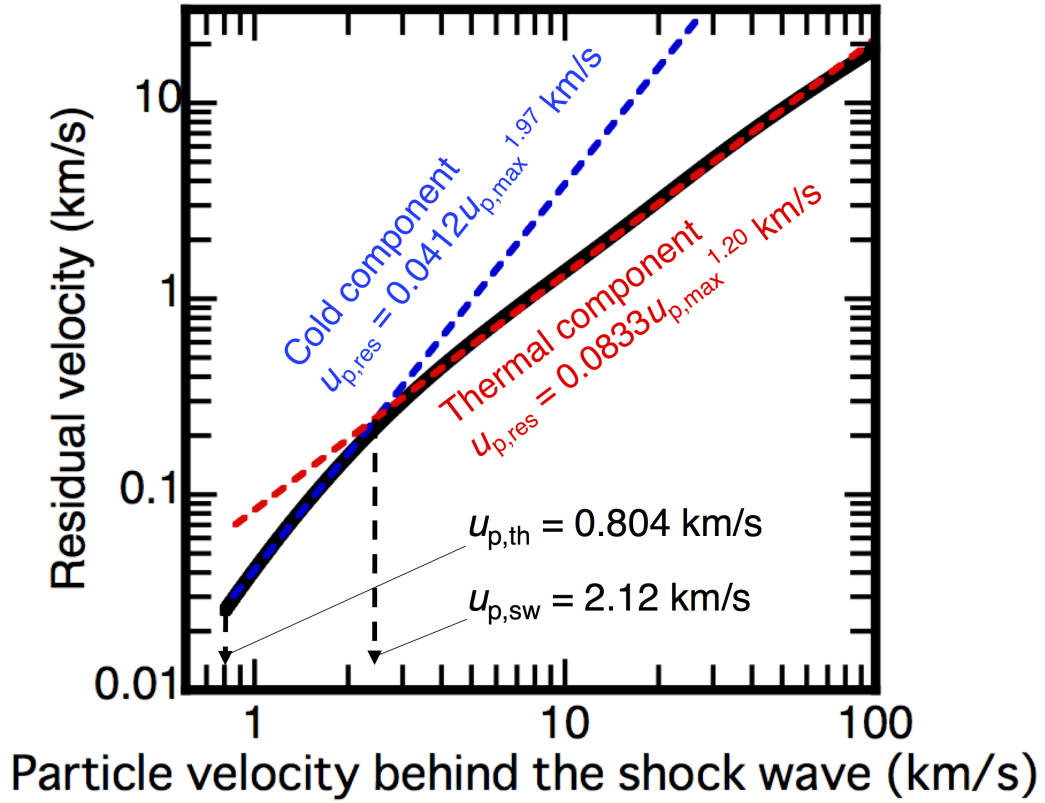


Figure 4: Residual velocity $u_{p,res}$ as a function of the peak particle velocity $u_{p,max}$ pertaining to granite. Two power-law functions, referred to as the thermal and cold components, are shown as dotted lines. The values of the switching and threshold velocities (see Section 3.1) are also included.

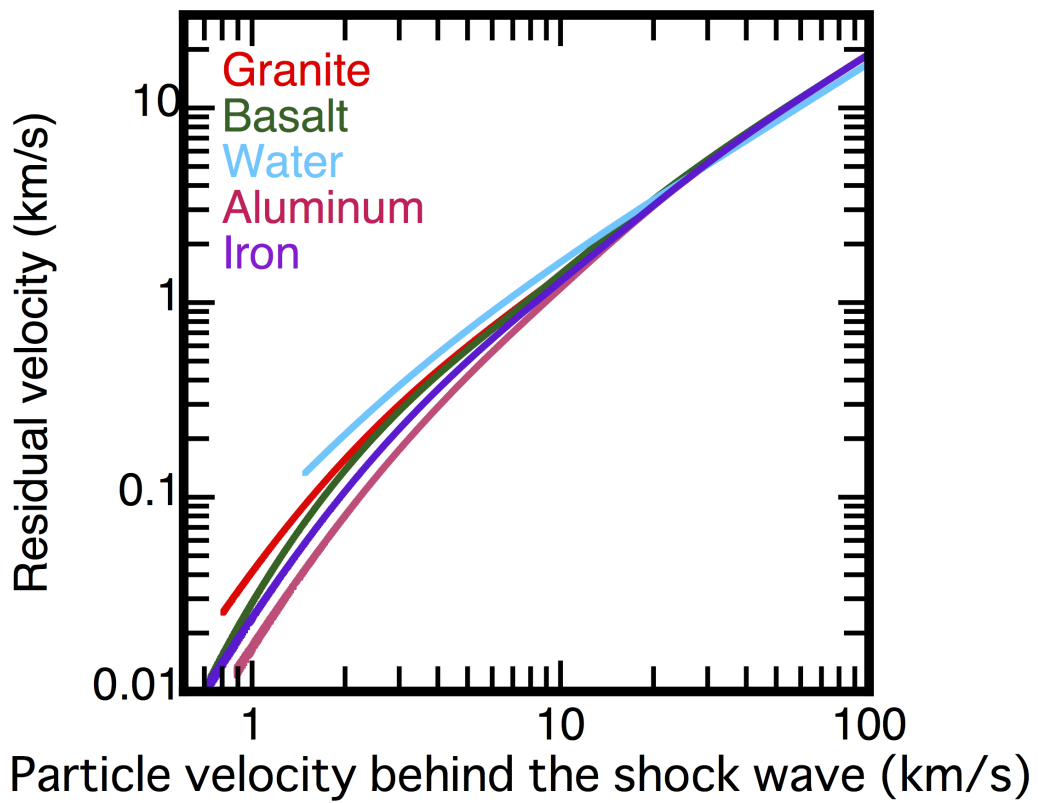


Figure 5: As for Fig. 4, but showing the relation between the residual velocity $u_{p,res}$ and the peak particle velocity $u_{p,max}$ for various materials.

The peak particle velocity $u_{p,\max}$ is also expressed as a power-law function [see Eq. (10)] with respect to the distance from the impact point r (for $r > R_p$). Thus, $u_{p,\text{res}}$ can be rewritten from Eq. (23) as a function of r , as follows:

$$u_{p,\text{res}} = C u_{p0}^m \left(\frac{r}{R_p} \right)^{-nm} \quad (r > R_p). \quad (26)$$

Analogously to the Maxwell Z -model, the exponent Z is related to the product of the exponents n and m . Since $n = 1.87$ (see Section 2.2) and $m > 1.2$ in most cases, except for m_t for water (Table 3.1), our model naturally reproduces $Z > 2$, which is the key constraint to describe streamlines (Section 2.1). Although we independently employed the values nm and Z from thermodynamic considerations [Eq. (26)] and Maxwell Z -model [(Eq. (7)), respectively, they are not mutually exclusive.

3.2. Energies in stream tubes

In this section, we describe the integrated results of Eqs. (16)–(19). Note that here we only show the proportional relations with dimensional constants from k_1 to k_9 . The expressions of the coefficients are presented in Appendix D. The total mass in a given streamtube is as follows (e.g., Maxwell, 1977):

$$M_{\text{tube}} = k_1 R^2 \Delta R, \quad (27)$$

When $u_{p0} > u_{p,\text{sw}}$, E_{kin} is divided into three terms:

$$E_{\text{kin}} = E_{\text{kin1}} + E_{\text{kin2}} + E_{\text{kin3}}, \quad (28)$$

where

$$E_{\text{kin1}} = k_2 u_{p0}^{2m_t} R_p^{Z+1} R^{-(Z-1)} \Delta R, \quad (29)$$

$$E_{\text{kin2}} = \left(k_3 u_{p0}^{2m_t} + k_4 u_{p0}^{\frac{Z+1}{n}} \right) R_p^{Z+1} R^{-(Z-1)} \Delta R, \quad (30)$$

and

$$E_{\text{kin}3} = k_5 u_{p0}^{\frac{Z+1}{n}} R_p^{Z+1} R^{-(Z-1)} \Delta R. \quad (31)$$

The contribution of the kinetic energy inside the isobaric core to the streamtube corresponds to $E_{\text{kin}1}$. The second and third terms ($E_{\text{kin}2}$ and $E_{\text{kin}3}$) originate mainly from the thermal pressure P_{thermal} (thermal component) and the cold pressure P_{cold} (cold component), respectively, on the outside of the isobaric core. Since $u_{p0} > u_{p,\text{sw}}$ was assumed in Eqs. (29)–(31), the kinetic energy of the material initially located inside the isobaric core $E_{\text{kin}1}$ is also classified as a thermal component. In contrast, if u_{p0} is slower than $u_{p,\text{sw}}$, the thermal component disappears:

$$E_{\text{kin}} = E_{\text{kin}1} + E_{\text{kin}2}, \quad (32)$$

where

$$E_{\text{kin}1} = k_6 u_{p0}^{2m_c} R_p^{Z+1} R^{-(Z-1)} \Delta R, \quad (33)$$

$$E_{\text{kin}2} = \left(k_7 u_{p0}^{2m_c} + k_8 u_{p0}^{\frac{Z+1}{n}} \right) R_p^{Z+1} R^{-(Z-1)} \Delta R. \quad (34)$$

Since u_{p0} is linearly proportional to v_{imp} , as discussed in Section 2.2, Eqs. (28)–(31) and (32)–(34) also include the dependence of v_{imp} on E_{kin} . The gravitational potential energy of a given streamtube E_{grav} is expressed as

$$E_{\text{grav}} = k_9 g R^3 \Delta R. \quad (35)$$

Figure 6 displays typical examples of the calculations, showing the kinetic energy and the gravitational potential energy in a given streamtube as a function of the horizontal distance R . A granite projectile and target were considered in these calculations. We set v_{imp} at 5 km s⁻¹ and 10 km s⁻¹ in

panels (a) and (b), respectively. To draw the figures, Z , g , and ΔR were set at 3, 1 G , and $10^{-4} R_p$, respectively. Since the u_{p0} velocities are higher than $u_{p,sw}$ in both cases, E_{kin1} and E_{kin2} are associated with the thermal component under the calculation conditions. All kinetic energy terms decrease following the power law, $E_{kin} \propto R^{-2}$: see Eqs. (29)–(31). E_{kin} and E_{grav} are balanced at $8.7 R_p$ and $13.2 R_p$ for $v_{imp} = 5 \text{ km s}^{-1}$ and 10 km s^{-1} , respectively. Although the gravitational potential energy increases more steeply with increasing R ($E_{grav} \propto R^3$; Eq. (35)), the deceleration owing to gravity can be neglected until the radius of the growing crater, $R_{cr}(t)$, approaches the transient crater radius. As discussed in the next section, $v_{ej}(R)$ and $R_{cr}(t)$ in the region where E_{grav} can be neglected exhibit the well-known power-law behavior.

Given that the yield strength is a constant and that the volumetric strain is approximated by unity as a first-order estimate, $E_{strength}$ is roughly approximated by

$$E_{strength} = \frac{M_{tube}}{\rho_t} Y = k_1 \left(\frac{Y}{\rho_t} \right) R^2 \Delta R. \quad (36)$$

Strictly speaking, the treatment of the material strength used above is affected by three main problems, as described in the remainder of this section. The first problem is that we neglect the effects of the velocity difference between the adjacent stream tubes to derive Eq. (20). The volumetric strain ε is essentially computed from the velocity difference. Thus, we assumed that the volumetric strain $\varepsilon = 1$ to calculate $E_{strength}$ is a first-order estimate, as mentioned above. The second problem is related to the first one; i.e., our neglect of the frictional behavior of geologic materials. Actual geologic media exhibit a complicated strength behavior because of dry friction (e.g., Lundborg, 1968). If the work done by the frictional drag force greatly

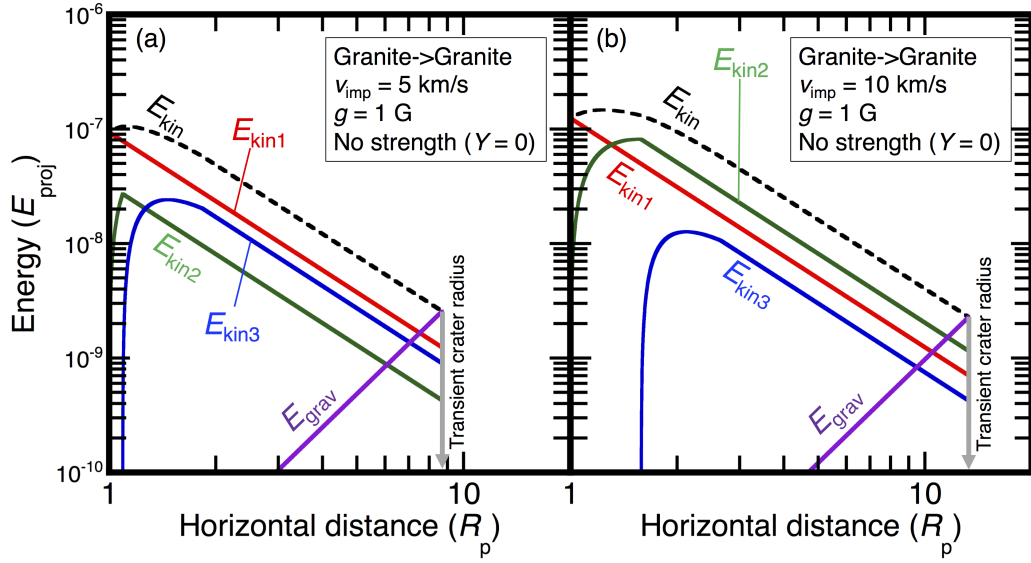


Figure 6: Horizontal profiles of kinetic energy and gravitational potential energy in a given streamtube. The impact velocity is (a) 5 km s^{-1} and (b) 10 km s^{-1} . The sum of the kinetic energies E_{kin} (black dashed line) of the thermal components $E_{\text{kin}1}$ (red solid line) and $E_{\text{kin}2}$ (green solid line), the cold component $E_{\text{kin}3}$ (blue solid line), as well as the gravitational potential energy E_{grav} (purple solid line) are plotted. The horizontal distance from the impact point R and the energies is normalized by the projectile radius R_p and the kinetic energy of the projectile E_{proj} .

affects the energy partitioning of the excavation flow, we cannot apply Eq. (20) to estimate the ejection velocity. Although we could in principle estimate the significance of the friction using numerical simulations with constitutive models, such advanced calculations are beyond the scope of this study. The final problem is the constant- Y assumption, which is only valid for metal-like targets. Despite this limitation, the constant- Y assumption has been widely used to derive the π -group scaling laws (e.g., Gault, 1973, Suzuki et al., 2012). Thus, we decided to present the cratering processes in the strength-dominated regime based on the constant- Y assumption. Because of these three simplifications, the predictions of our model regarding the impact outcomes in the strength-dominated regime are expected to be associated with significant uncertainties in this regime.

3.3. Ejection behavior

In this section, we discuss the ejecta characteristics pertaining to our model. Figure 7 shows examples of crater growth in the gravity-dominated regime ($E_{\text{grav}} \gg E_{\text{strength}}$) calculated using Eqs. (20)–(22), (28), and (35). We assumed that a granite projectile of 1 m in radius collides with a strengthless granite target at 10 km s^{-1} under a gravitational acceleration $g = 1 \text{ G} = 9.81 \text{ m s}^{-2}$. Three different Z values were used (2.5, 3.0, and 3.5). Normalized radii of the growing craters $R_n = (\rho_p/M_p)^{1/3} R_{\text{cr}}$ are plotted against a normalized time quantity, $t_n = t/t_s$. Crater growth under these conditions follows a power law before $t_n \simeq 10^4$. Next, the growth rates gradually decrease with time, and they cease around $t_n \simeq 10^5$. Although the absolute value of the timing of the material ejection (x axis) is a first-order estimate, as mentioned in Section 2.3, because of the uncertainty in the characteristic

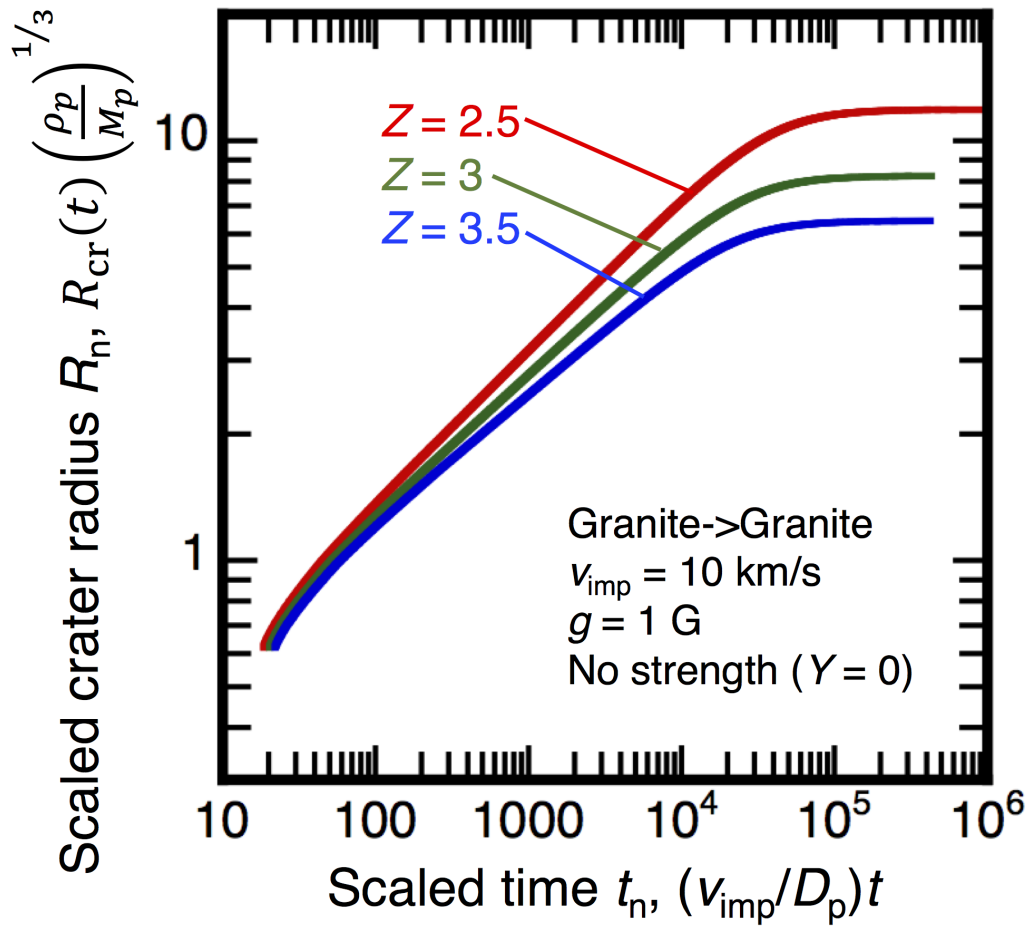


Figure 7: Time variation of the radii of growing craters. The relevant conditions are listed in the figure. Both the crater radii and the time after impact are normalized so as to be dimensionless variables. Results are shown for $Z = 2.5$ (red), 3.0 (green), and 3.5 (blue).

velocity of the material in a given streamtube, the time sequence is consistent with those derived in previous experimental studies (e.g., Yamamoto et al., 2009, 2017). The power-law exponent depends on Z . Our model naturally reproduces the power-law behavior, as follows. The ejection velocity v_{ej} under the condition where $E_{\text{kin}} \gg E_{\text{grav}}$ (and/or E_{strength}), which actually holds in our model (see Fig. 6), is practically equal to

$$v_{\text{ej}} = \sqrt{\frac{2E_{\text{kin}}}{M_{\text{tube}}}}. \quad (37)$$

In this case, the ejection velocity distribution (i.e., v_{ej} as a function of R) and the time variation of R_{cr} can be expressed as power-law functions as follows:

$$v_{\text{ej}} \propto R^{-\frac{Z+1}{2}}, \quad (38)$$

and

$$R_{\text{cr}} \propto t^{\frac{2}{Z+3}}. \quad (39)$$

Figure 8 shows the ejecta velocity distributions. We calculated the ejection velocity and the ejecta volume launched at a higher velocity than a given ejection velocity using the same calculations as those in Fig. 7. Following Housen et al. (1983), we plotted the normalized ejection velocity $v_{\text{ej}}/\sqrt{gR_{\text{tr}}}$ as a function of both the normalized ejecta position R/R_{tr} (Fig. 8a) and the scaled ejecta volume $V(> v_{\text{ej}})/R_{\text{tr}}^3$ (Fig. 8b). To compare with previous results, the best-fitting lines from Housen et al. (1983), based on point-source theory, are also plotted. As described by Eq. (38), the scaled ejection velocities exhibit power-law behaviors that depend on Z (Fig. 8a). For $Z = 3.5$, the slope is close to the best-fit line of Housen et al. (1983). The difference in the absolute value between the line for $Z = 3.5$ and the best-fit line

(blue solid and dotted lines, respectively) might originate from the fact that the best-fit line was determined using the final crater radii rather than the transient crater radii. The line for $Z = 3.5$ is consistent with the result of Housen et al. (1983) in terms of the ejecta volume at a given ejection velocity (Fig. 8b). The scaled ejecta volume deviates from the power law (the dotted line) in regions characterized by relatively high and low scaled ejection velocities. This behavior is consistent with previous numerical results obtained by Wada et al. (2006). Since the validity of Eq. (37) breaks down at relatively low ejection velocities (i.e., $E_{\text{kin}} \sim E_{\text{grav}}$), the results deviate from the power-law behavior. A cut-off at high ejection velocities is discussed in detail in Section 4.2. Consequently, our model predicts a similar power-law behavior as that proposed in previous studies (e.g., Housen et al., 1983, Schmidt and Housen, 1987). The correspondence between our model and the point-source theory is discussed in Section 4.3.

3.4. Transient crater radii

The transient crater radius R_{tr} in the gravity-dominated regime, defined as $E_{\text{grav}} \gg E_{\text{strength}}$, is obtained by assuming $E_{\text{kin}} = E_{\text{grav}}$, so that

$$R_{\text{tr}} = R_{\text{p}}^{\frac{Z+1}{Z+2}} (k_9 g)^{-\frac{1}{Z+2}} \left[(k_2 + k_3) u_{\text{p0}}^{2m_t} + (k_4 + k_5) u_{\text{p0}}^{\frac{Z+1}{n}} \right]^{\frac{1}{Z+2}} \quad (\text{if } u_{\text{p0}} > u_{\text{p,sw}}), \quad (40)$$

and

$$R_{\text{tr}} = R_{\text{p}}^{\frac{Z+1}{Z+2}} (k_9 g)^{-\frac{1}{Z+2}} \left[(k_6 + k_7) u_{\text{p0}}^{2m_c} + k_8 u_{\text{p0}}^{\frac{Z+1}{n}} \right]^{\frac{1}{Z+2}} \quad (\text{if } u_{\text{p0}} < u_{\text{p,sw}}). \quad (41)$$

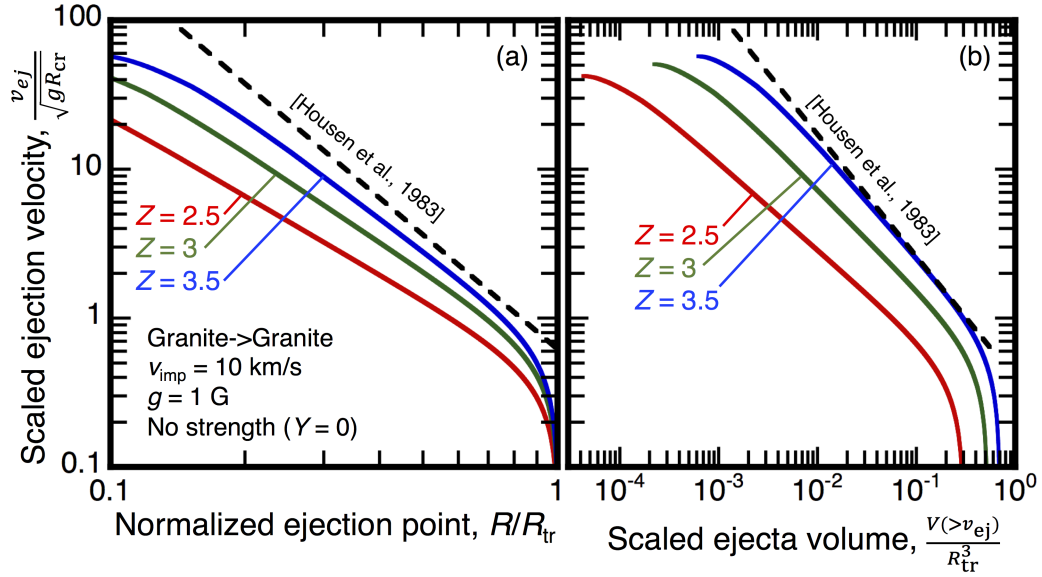


Figure 8: (a) Ejecta velocity distribution and (b) relation between the cumulative volume of the ejecta launched at a given ejection velocity and the ejection velocity. These results are obtained from the same calculation as that shown in Fig. 7. The previous ejecta scaling laws of Housen et al. (1983), (a) $\frac{v_{ej}}{\sqrt{gR_{tr}}} = 0.62 \left(\frac{R}{R_{tr}}\right)^{-2.55}$ and (b) $\frac{V(>v_{ej})}{R_{tr}^3} = 0.32 \left(\frac{v_{ej}}{\sqrt{gR_{tr}}}\right)^{-1.22}$, are also shown (dotted lines).

In the strength-dominated regime (i.e., $E_{\text{grav}} \ll E_{\text{strength}}$), R_{tr} is calculated by assuming $E_{\text{kin}} = E_{\text{strength}}$, so that

$$R_{\text{tr}} = R_{\text{p}} \left(\frac{k_1 Y}{\rho_t} \right)^{-\frac{1}{Z+1}} \left[(k_2 + k_3) u_{\text{p0}}^{2m_t} + (k_4 + k_5) u_{\text{p0}}^{\frac{Z+1}{n}} \right]^{\frac{1}{Z+1}} \quad (\text{if } u_{\text{p0}} > u_{\text{p,sw}}), \quad (42)$$

and

$$R_{\text{tr}} = R_{\text{p}} \left(\frac{k_1 Y}{\rho_t} \right)^{-\frac{1}{Z+1}} \left[(k_6 + k_7) u_{\text{p0}}^{2m_c} + k_8 u_{\text{p0}}^{\frac{Z+1}{n}} \right]^{\frac{1}{Z+1}} \quad (\text{if } u_{\text{p0}} > u_{\text{p,sw}}). \quad (43)$$

Of note, R_{tr} in our model depends on the exponents n and m , indicating that the nature of the decaying shock propagation and the thermodynamic/hydrodynamic response of geological materials are included to predict the resulting crater sizes.

Figures 9–11 show R_{tr} resulting from our model in the form of π -group scaling laws, along with the conventional results. A granite projectile and target were considered. We calculated the scaled crater diameter π_D (Y axis) and the gravity-scaled size π_2 (X axis). We focused on the Z , v_{imp} , and Y dependences on π_D in Figs. 9–11, respectively. In Fig. 9, Z was varied from 2.01 to 4, v_{imp} was fixed at 10 km s^{-1} , and no strength ($Y = 0$) was included. Although our prediction is sensitive to the exponent Z , the resulting π_D values predicted by our model are contained within the two typical scaling lines pertaining to saturated soil and dry quartz sand (Schmidt and Housen, 1987), thereby strongly supporting the notion that our model accurately predicts transient crater radii. The differences in the materials for the conventional scaling laws correspond to the differences in Z in our model. In Fig. 10, v_{imp} was varied from 5 to 100 km s^{-1} , Z was fixed at 3, and no strength ($Y = 0$) was included. The different v_{imp} values yield different π_D values within a

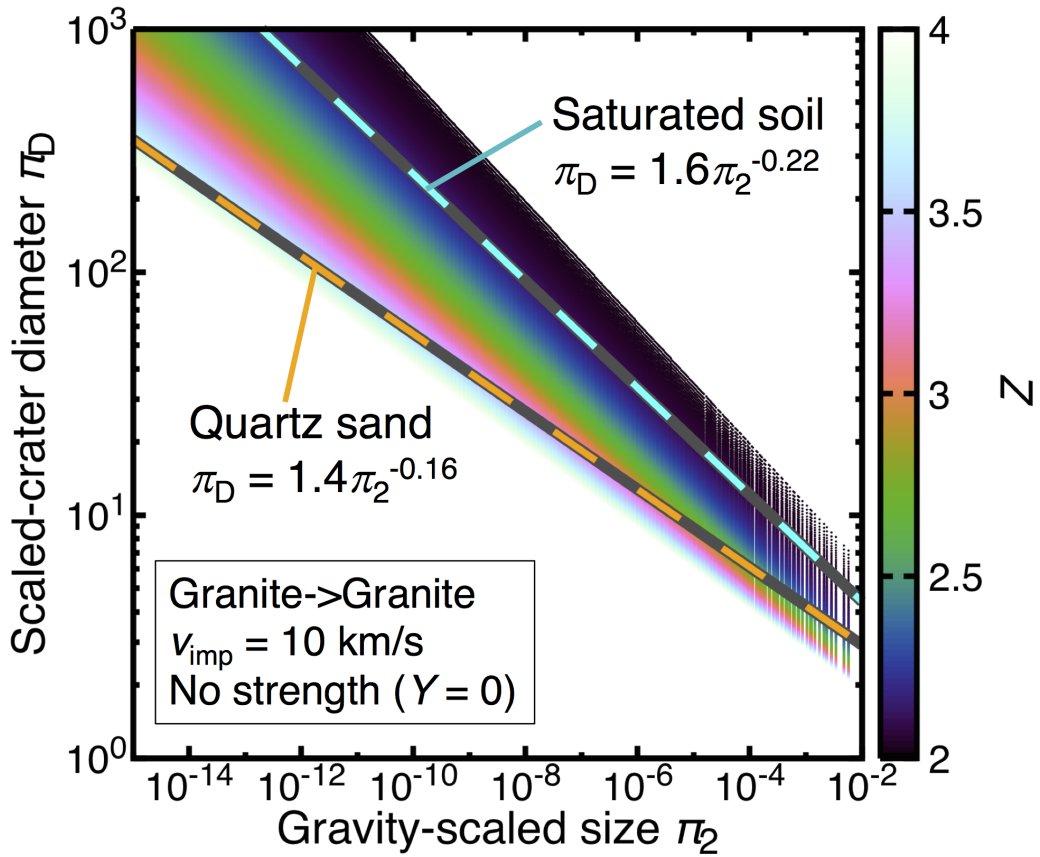


Figure 9: Scaled crater diameter π_D as a function of π_2 . The calculated π_D values are colored depending on the exponent Z . The other calculation conditions are also indicated in the figure. Two typical scaling lines for saturated soil (cyan) and dry quartz sand (orange) are shown. The scaling constant and exponent are from Schmidt and Housen (1987).

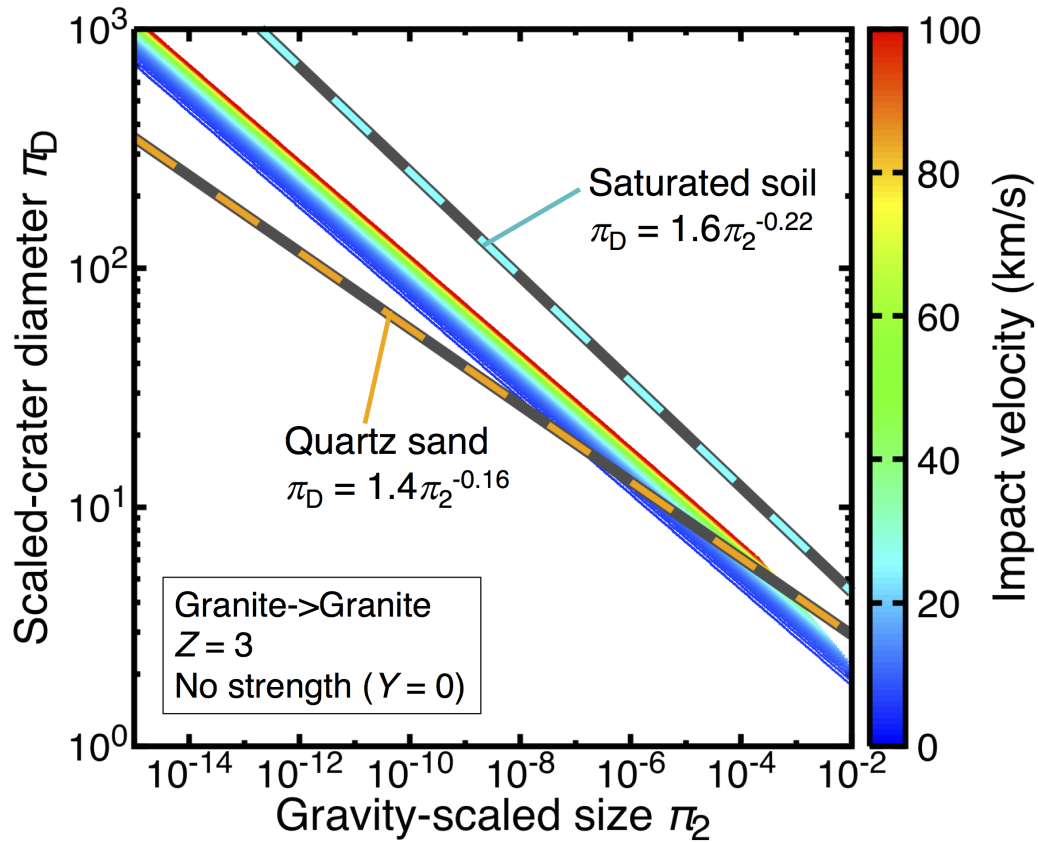


Figure 10: As for Fig. 9, except that the calculated π_D values are colored depending on the impact velocity.

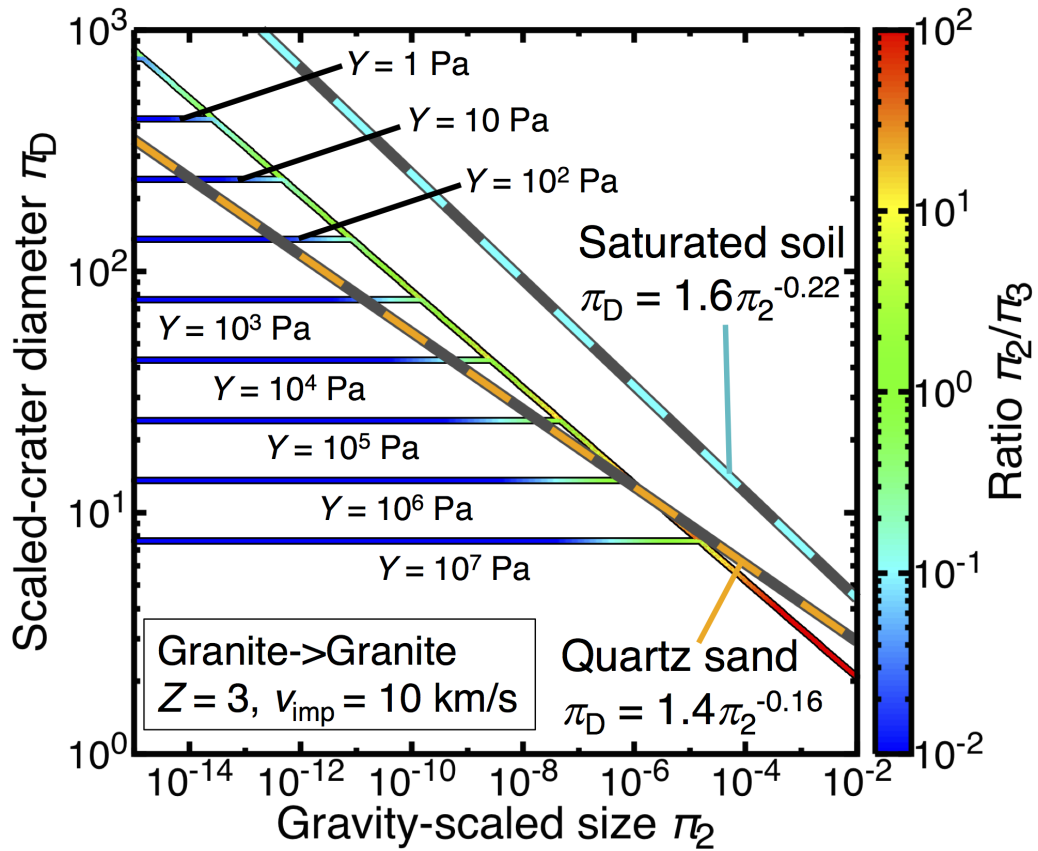


Figure 11: As for Figs. 9 and 10, but showing the effect of the strength Y on the π_D behavior versus π_2 . The scaled crater diameters are colored according to the ratio of π_2 to π_3 .

factor of 1.6 for the same value of π_2 , suggesting that π_2 would not be a good measure to define the scale of impact events in terms of the v_{imp} dependence. The reason for this result is discussed in Section 4.4. In Fig. 11, Y was varied from 1 Pa to 10^7 Pa, v_{imp} was fixed at 10 km s^{-1} , and Z was fixed at 3 to investigate the transition behavior from the gravity-dominated to the strength-dominated regime with decreasing π_2 . In this calculation, we determined R_{tr} based on $\min(R_{\text{tr,grav}}, R_{\text{tr,strength}})$, where $R_{\text{tr,grav}}$ and $R_{\text{tr,strength}}$ are the transient crater radii calculated using Eqs. (40) and (42), respectively. The effect of material strength on crater formation becomes dominant when the ratio of π_2 to π_3 falls below 0.1.

4. Discussion

4.1. A verification via hydrocode modeling

Here we discuss the limitations of our model. We assumed that the residual velocity is zero when $u_{\text{p,max}} < u_{\text{p,th}}$. Thus, the model predicts that no craters are produced for low-velocity impacts, regardless of the strength of the target material. This obviously contradicts the well-known fact that low-velocity impacts also produce impact craters when the target materials have relatively low strength. To address the limitations of the key assumption of the model that the residual velocity after a shock-release cycle is the origin of the excavation flow, we also perform a numerical simulation based on the iSALE shock physics code (Amsden et al., 1980, Ivanov et al., 1997, Wünnemann et al., 2006). The results are described in the Supplementary Information. We confirmed that our analytical result (thick black line in Fig. 4) reproduces well the numerical results in the thermal-pressure-dominated

range (red dashed line in Fig. 4). The $u_{p,res}$ in the cold-pressure-dominated regime (blue dashed line in Fig. 4) is, however, considerably slower than the numerical results. This result indicates a difference in the physics underlying the formation of an excavation flow during low-velocity impacts compared with that during the hypervelocity impacts discussed in this study. Consequently, the accuracy of the model prediction is relatively high in the thermal-pressure-dominated regime, which roughly corresponds to the condition $v_{imp} > 2u_{p,sw}$ (typically $v_{imp} > 5 \text{ km s}^{-1}$), although it would predict somewhat slower ejection velocities and smaller transient craters in the cold-pressure-dominated regime. Our model is therefore suitable for predicting impact outcomes after hypervelocity impact events on Mars-sized or larger planets, their satellites, and after typical collisions between asteroids in the main-belt region.

4.2. High-speed cut-off of the ejection velocity in the normal excavation process

It is widely considered that impact excavation can be divided into three stages depending on ejection timing, location, velocity, and pressure: (1) jetting, (2) spallation, and (3) normal excavation (e.g., Melosh, 1989, Kurosawa et al., 2018). The transition behaviors from jetting to spallation to normal excavation have been summarized by Kurosawa et al. (2018). In this study, we have discussed normal excavation. The ejecta velocity distribution owing to normal excavation is expressed as a power-law relation, as discussed in Section 3.3. However, a high-speed cut-off $v_{ej,max}$ is required because the total kinetic energy carried away by the ejecta becomes infinite without such a cut-off (Housen and Holsapple, 2011). A higher ejection velocity than the cut-off

value can be achieved by jetting and/or spallation (e.g., Melosh and Sonett, 1986, Vickery, 1993, Johnson et al., 2014, Kurosawa et al., 2015, 2018). Our model, which was constructed based on the framework initially proposed by Melosh (1985), clearly predicts the residual velocity in the isobaric core to be at the high-speed cut-off; i.e., $v_{\text{ejmax}} = Cu_{\text{p0}}^m$. The cut-off is typically 4%–20% of v_{imp} (Fig. 4).

4.3. Correspondence between the proposed model and conventional scaling laws

The ejecta velocity distribution and crater growth have been discussed in terms of the point-source theory (e.g., Housen et al., 1983, Holsapple, 1993). By comparing Eq. (38) and the predictions of point-source theory, Z is expressed as a function of the velocity-scaling exponent μ as follows:

$$Z = \frac{2 - \mu}{\mu}. \quad (44)$$

Since the allowable μ range spans from 1/3 (momentum scaling) to 2/3 (energy scaling) as discussed in Section 1, Z is estimated to range from 2 to 5. This range is consistent with the value of the product nm (Table 3.1), and these might be reasonable values to describe a cratering flow field (e.g., Croft, 1980, Melosh, 1989). Note that the relationship between μ and Z is frequently given by (e.g., Housen et al., 1983)

$$Z = \frac{1}{\mu}. \quad (45)$$

for the frequently used assumptions discussed in Section 2.1; i.e., the time-dependent strength of the excavation flow $\alpha(t) = \text{Const}$. The difference in the relationship between Eqs. (44) and (45) implies that our model implicitly

assumes a time-dependent $\alpha(t)$, although we do not necessarily explicitly address the functional form of $\alpha(t)$. Since the shapes of the streamlines of the excavation flow depend only on the exponent Z in the Z -model (Eq. (8)), we were able to formulate the equations related to the cratering processes without an explicit expression for $\alpha(t)$. In situ observations of the growth of the crater radius $R_{\text{cr}}(t)$ in a laboratory setting allows us to determine the exponents μ and Z for each impact (e.g., Yamamoto et al., 2009, 2017). The crater radius as a function of time is expressed as follows:

$$R_{\text{cr}}(t) \propto t^{e_x}, \quad (46)$$

where e_x is an exponent determined from laboratory measurements (Cintala et al., 1999). By comparison with Eq. (39), the exponent Z is related to e_x as

$$Z = \frac{2 - 3e_x}{e_x}. \quad (47)$$

If we assume Z to range from 2 to 5, as discussed above, e_x becomes 0.25–0.40. The range of e_x is consistent with the values of e_x measured in laboratory experiments with dry sand targets (Cintala et al., 1999, Yamamoto et al., 2017).

4.4. Modified measure of the gravity-scaled size

Here, we discuss the effect of v_{imp} on π_D and the gravity-scaled size π_2 . First, we obtain the transient crater radius R_{tr} in the framework of the π -group scaling laws from Eqs. (2), (3), and (6) to directly compare with our model [Eqs. (40) and (41)]. In the case of collisions between the same materials (i.e., $\rho_p = \rho_t$ and $2u_{p0} = v_{\text{imp}}$), R_{tr} is rewritten as

$$R_{\text{tr}} = k_{10} R_p^{1-\beta} g^{-\beta} u_{p0}^{2\beta}, \quad (48)$$

where k_{10} is a dimensionless constant described in Appendix D and

$$\beta = \frac{\mu}{\mu + 2} = \frac{1}{Z + 2}. \quad (49)$$

Note that we used Eq. (6) to obtain Eq. (49). Thus, the dependences of R_p and g on R_{tr} in our model are consistent with the π -group scaling laws when Eq. (49) is valid. In contrast, the u_{p0} dependence on R_{tr} is quite different, as shown in Eqs. (40), (41), and (48), which is expected to produce factor 1.6 dispersion against the same π_2 values in our model shown in Fig. 9.

Second, we discuss the origin of the difference in the u_{p0} dependence on R_{tr} . Since the residual velocity ultimately originates from irreversible shock heating (i.e., an increase in entropy), as discussed in Section 2, the conversion efficiency from the initial kinetic energy injected by the projectile E_{proj} to the total kinetic energy in the excavation flow E_{res} is expected to strongly depend on v_{imp} . When u_{p0} is greater than $u_{p,sw}$, E_{res} is divided into three terms in the same way as used in the derivation of E_{kin} :

$$E_{res} = E_{res1} + E_{res2} + E_{res3}, \quad (50)$$

where

$$E_{res1} = k_{11} u_{p0}^{2m_t} R_p^3, \quad (51)$$

$$E_{res2} = k_{12} u_{p0}^{2m_t} R_p^{2nm_t}, \quad (52)$$

$$E_{res3} = k_{13} u_{p0}^{2m_c} R_p^{2nm_c}. \quad (53)$$

If $u_{p0} < u_{p,sw}$, E_{res} is expressed as

$$E_{res} = E_{res1} + E_{res2}, \quad (54)$$

where

$$E_{\text{res1}} = k_{14} u_{\text{p0}}^{2m_c} R_{\text{p}}^3, \quad (55)$$

and

$$E_{\text{res2}} = k_{15} u_{\text{p0}}^{2m_c} R_{\text{p}}^{2nm_c}. \quad (56)$$

As in Section 3.2, we only show the proportional relations with dimensional constants k_{11} – k_{15} . The explicit expressions of the coefficients are presented in Appendix D. Since u_{p0} is linearly proportional to v_{imp} (e.g., Melosh, 1989), E_{res} is not expressed as a simple linear function of $E_{\text{proj}} = M_{\text{p}} v_{\text{imp}}^2 / 2$. Consequently, π_D is not fully scaled by the gravity-scaled size in our model (Fig. 10). In light of our key assumption (i.e., that the excavation flow is driven by the residual velocity of the shocked materials) (Melosh, 1985), we propose a modified expression of the gravity-scaled size as follows:

$$\pi_{2\text{mod}} = \frac{1}{16} \left(\frac{4\pi}{3} \right)^{\frac{4}{3}} \frac{\rho_{\text{p}} g D_{\text{p}}^4}{E_{\text{res}}} = \frac{0.42 \rho_{\text{p}} g D_{\text{p}}^4}{E_{\text{res}}}. \quad (57)$$

We simply used E_{res} here instead of E_{proj} in the original form of π_2 [Eq. (3)].

4.5. Insights into future laboratory/numerical experiments

The proposed model is one of the simplest methods to predict the crater size when Tillotson EOS parameters are available. The Tillotson parameters can be obtained if the shock Hugoniot parameters are available (e.g., Melosh, 1989). Since both laboratory and numerical impact experiments are expensive and time-consuming, the new method could serve as a quick-look tool pertaining to crater size and would significantly aid in the design of laboratory and numerical experiments. An advantage of the new model is that the mechanics of the impact cratering processes, which cannot be addressed by

dimensional analysis, are considered. This allows us to predict the tendencies of the impact outcomes as a function of a range of variables, as discussed below.

The dimensionless parameters, including the internal friction f and the porosity ϕ , could in principle be incorporated into our model in a straightforward manner. The decay exponent n is expected to become larger with increasing f and ϕ (e.g., Mitani, 2003, Wünnemann et al., 2006, Bierhaus et al., 2013, Nagaki et al., 2016). The exponent m is also expected to change and depend on ϕ , because ϕ affects the degree of irreversible shock heating (e.g., Ahrens and O’Keefe, 1972, Wünnemann et al., 2008). The effects of f and ϕ on both crater size and the ejecta velocity distribution would appear as a change in Z in our model, because Z is possibly controlled by the product nm , as discussed in Section 3.1. Prieur et al. (2017) examined the effects of f and ϕ on the transient crater size based on a number of numerical experiments, and they presented empirical equations pertaining to μ as functions of f and ϕ . Similar numerical experiments, focusing on the effects of f and ϕ on the exponents n , m , and Z using a shock physics code, may be useful in obtaining a physical interpretation of the empirical equations.

Recent impact experiments performed by Yamamoto et al. (2017) suggest that the velocity-scaling exponent μ also depends on v_{imp} . They concluded that a higher v_{imp} tends to lead to a lower μ . This experimental result is understandable if the assumption $Z \sim nm$ is correct, as explained below. Although the exponent n was treated as a constant $n = 1.87$ throughout this study, the shock decay exponent n is weakly dependent on v_{imp} . According to a series of hydrocode simulations (Pierazzo et al., 1997), a higher v_{imp} leads

to a larger n , implying that a higher v_{imp} leads to a smaller μ because μ is related to Z [Eq. (44)]. This hypothesis is consistent with the experimental results of Yamamoto et al. (2017). A larger v_{imp} , however, also causes a smaller m ($m_t < m_c$). Thus, a complex behavior of μ as a function of v_{imp} is expected in reality. Further discussion of the v_{imp} dependence of μ is beyond the scope of this study. Numerical simulations would significantly contribute to solving this problem.

5. Conclusion

We have proposed a model to predict impact outcomes by combining the Maxwell Z -model and the residual velocity. In this study, we omitted some physics behind the cratering processes, such as the gradual change in the velocity vectors of the excavating target materials after a shock-release cycle, the neglect of the effects of velocity difference between adjacent stream tubes, and metal-like targets with a constant yield strength Y . These simplifications allowed us to obtain analytical solutions. The new model allows us to analytically calculate the ejecta velocity distribution, the time variation of crater radii, and transient crater radii for a given impact condition based on a set of input parameters, including the exponents Z , n , and m . By analogy with the Maxwell Z -model, we propose that the exponent Z , which controls the shapes of streamlines in the excavation flow, is related to the product of the exponents n and m . Our model is combined with the widely used point-source theory through the relation between Z and the velocity-scaling exponent μ . The impact outcomes predicted by the new model seem to yield reasonable trends compared with previous results. The new analytical model

could aid in the design of a future interactive study comparing laboratory and numerical experiments to obtain a better understanding of the controls on impact outcomes.

Acknowledgements

We thank Hiroki Senshu for useful discussions. We also thank the developers of iSALE, including G. Collins, K. Wünnemann, B. Ivanov, J. Melosh, and D. Elbeshausen. We appreciate the suggestions by Boris Ivanov that helped us greatly improve the manuscript, and we thank Oded Aharonson for handling of this manuscript as the journal editor. We also acknowledge useful discussions at a workshop on planetary impacts held at Kobe University. KK is supported by JSPS KAKENHI Grant Nos. 17H01176, 17H02990, 17H01175, and 17K18812. ST is supported by JSPS KAKENHI Grant No. 16H06478.

Appendix A. Expressions of the thermal and cold pressures, P_{thermal} and P_{cold}

We employed the Tillotson EOS to calculate the residual velocity, as discussed in Section 2.2. The thermal and cold pressures, P_{thermal} and P_{cold} , are given by (Tillotson, 1962)

$$P_{\text{thermal}}(E, \rho) = \left[a + \frac{b}{\left(\frac{E}{E_0 \eta^2} + 1 \right)} \right] \rho E, \quad (\text{A.1})$$

and

$$P_{\text{cold}}(\rho) = A\mu + B\mu^2, \quad (\text{A.2})$$

where $\eta = \frac{\rho}{\rho_0}$, $\mu = \rho - 1$, and a , b , A , B , and E_0 are the Tillotson parameters.

Appendix B. Expression of $f(Z)$

From simple geometric considerations, the geometric factor $f(Z)$, which is the ratio of the total travel distance L along a given streamline to the horizontal distance R from the impact point, is expressed as

$$f(Z) = \int_0^{\frac{\pi}{2}} \sqrt{\left(\frac{\sin \theta}{Z-2}\right)^2 (1 - \cos \theta)^{\frac{2(3-Z)}{Z-2}} + (1 - \cos \theta)^{\frac{2}{Z-2}}} d\theta. \quad (\text{B.1})$$

Appendix C. Definition of the threshold velocity, $u_{p,\text{th}}$

We assumed that the residual velocity $u_{p,\text{res}}$ is zero when the peak particle velocity $u_{p,\text{max}}$ is slower than the threshold velocity $u_{p,\text{th}}$. In other words, our model is only valid when the hypersonic condition applies, which corresponds to the condition that the wave speed U is higher than the longitudinal sound speed C_L . This definition is the same as that employed in a previous study (Melosh, 1989, p. 38, fig. 3.7)]. The threshold velocity $u_{p,\text{th}}$ is estimated by application of the widely used linear velocity relation (e.g., Melosh, 1989), $U = C_0 + s u_{p,\text{max}}$. Thus, $u_{p,\text{th}}$ is approximated as

$$u_{p,\text{th}} = \frac{C_L - C_0}{s}. \quad (\text{C.1})$$

Appendix D. Explicit expressions of the coefficients

Here, we describe the coefficients from k_1 to k_{15} . The definitions of the variables are described in the main text.

$$k_1 = 2\pi \left(\frac{Z-2}{Z+1} \right) \rho_t, \quad (\text{D.1})$$

$$k_2 = \pi \left(\frac{Z-2}{Z+1} \right) \rho_t C_t^2, \quad (\text{D.2})$$

$$k_3 = \pi \left(\frac{Z-2}{2nm_t - Z - 1} \right) \rho_t C_t^2, \quad (\text{D.3})$$

$$k_4 = k_3 u_{\text{p,sw}}^{\frac{2nm_t - Z - 1}{n}}, \quad (\text{D.4})$$

$$k_5 = \pi \left(\frac{Z-2}{2nm_c - Z - 1} \right) \rho_t C_c^2 \left(u_{\text{p,sw}}^{\frac{2nm_c - Z - 1}{n}} - u_{\text{p,th}}^{\frac{2nm_c - Z - 1}{n}} \right), \quad (\text{D.5})$$

$$k_6 = \pi \left(\frac{Z-2}{Z+1} \right) \rho_t C_c^2, \quad (\text{D.6})$$

$$k_7 = \pi \left(\frac{Z-2}{2nm_c - Z - 1} \right) \rho_t C_c^2, \quad (\text{D.7})$$

$$k_8 = k_7 u_{\text{p,th}}^{\frac{2nm_c - Z - 1}{n}}, \quad (\text{D.8})$$

$$k_9 = \pi \left[\frac{Z^2 - 4Z + 4}{Z(Z+2)} \right] \rho_t, \quad (\text{D.9})$$

$$k_{10} = 4^\beta \left(\frac{4\pi}{3} \right)^{\frac{1-\beta}{3}} K_1, \quad (\text{D.10})$$

$$k_{11} = \frac{\pi}{3} \rho_t C_t^2, \quad (\text{D.11})$$

$$k_{12} = \frac{\pi}{2nm_t - 3} \rho_t C_t^2 \left(R_{\text{p}}^{-(2nm_t-3)} - R_{\text{sw}}^{-(2nm_t-3)} \right), \quad (\text{D.12})$$

$$k_{13} = \frac{\pi}{2nm_c - 3} \rho_t C_c^2 \left(R_{\text{sw}}^{-(2nm_c-3)} - R_{\text{th}}^{-(2nm_c-3)} \right), \quad (\text{D.13})$$

$$k_{14} = \frac{\pi}{3} \rho_t C_c^2, \quad (\text{D.14})$$

and

$$k_{15} = \frac{\pi}{2nm_c - 3} \rho_t C_c^2 \left(R_{\text{p}}^{-(2nm_c-3)} - R_{\text{th}}^{-(2nm_c-3)} \right), \quad (\text{D.15})$$

where

$$R_{\text{sw}} = R_{\text{p}} \left(\frac{u_{\text{p0}}}{u_{\text{p,sw}}} \right)^{\frac{1}{n}}, \quad (\text{D.16})$$

and

$$R_{\text{th}} = R_{\text{p}} \left(\frac{u_{\text{p0}}}{u_{\text{p,th}}} \right)^{\frac{1}{n}}. \quad (\text{D.17})$$

References

- Ahrens, T. J., O’Keefe, J. D. 1972. Shock melting and vaporization of lunar rocks and materials. *The Moon* **4**, 214–249.
- Amsden, A., Ruppel, H., Hirt, C., 1980. SALE: A simplified ALE computer program for fluid flow at all speeds. Los Alamos National Laboratories Report, LA-8095:101p.
- Baldwin, E. C., Milner, D. J., Burchell, M. J., and Crawford, I. A. 2007. Laboratory impacts into dry and wet sandstone with and without an over-lying water layer: Implications for scaling laws and projectile survivability. *Meteorit. Planet. Sci.*, **42**, 1905–1914, doi:10.1111/j.1945- 5100.2007.tb00549.x.
- Barnouin-Jha, O. S., Yamamoto, S., Toriumi, T., Sugita, S., and Matsui, T. 2007. Non-intrusive measurements of crater growth. *Icarus* **188**, 506–521.
- Benz, W. and Asphaug, E. 1999. Catastrophic disruption revisited. *Icarus* **142**, 5–20.
- Buckingham, E. 1914. On physically similar systems; illustrations of the use of dimensional equations. *Phys. Rev.*, **4**(4), 345.

- Bierhaus, M., Wünnemann, K., Ivanov, B. 2013. Affect of core rheology on shock wave propagation in planetary scale impacts. *Large Meteorite Impacts and Planetary Evolution V* #3022.
- Cintala, M. J., Berthoud, L., and Hörz, F. 1999. Ejection-velocity distributions from impacts into coarse-grained sand. *Meteorit. Planet. Sci.* **34**, 605–623, doi:10.1111/j.1945-5100.1999.tb01367.x.
- Croft, S. K., 1980. Cratering flow fields-implications for the excavation and transient expansion stages of crater formation. In: *Proc. Lunar and Planetary Science Conference 11th*, pp. 2347–2378.
- Croft, S. K., 1982. A first-order estimate of shock heating and vaporization in oceanic impacts. *Geol. Soc. Am. Spec. Papers* **190**, 143–152, doi:10.1130/SPE190-p143.
- Dienes, J. K., and Walsh, J. M., 1970. Theory of impact: Some general principles and the method of Eulerian codes. in *High-Velocity Impact Phenomena*, edited R. Kinslow, pp. 46–104, Academic Press, New York.
- Elbeshausen, D., Wünnemann, K., and Collins, G. S., 2009. Scaling of oblique impacts in frictional targets: Implications for crater size and formation mechanisms. *Icarus* **204**, 716–731, doi:10.1016/j.icarus.2009.07.018
- Fassett, C. I., 2016. Analysis of impact crater populations and the geochronology of planetary surfaces in the inner solar system. *Journal of Geophysical Research: Planets* **121**, 1900–1926, doi:10.1002/2016JE005094.
- Gault, D. E., 1973. Displaced mass, depth, diameter, and effects of oblique

- trajectories for impact craters formed in dense crystalline rocks. *The Moon* **6**, 32–44, doi:10.1007/BF02630651.
- Gault, D. E., and Wedekind, J. A. 1977. Experimental hypervelocity impact into quartz sandII: Effects of gravitational acceleration, paper presented at Impact and Explosion Cratering: Planetary and Terrestrial Implications; Proceedings of the Symposium on Planetary Cratering Mechanics, Flagstaff, Ariz., September 13–17, 1976. (A78–44030 19–91), Pergamon Press, New York.
- Güldemeister, N., Wünnemann, K., and Poelchau, M., 2015. Scaling impact crater dimensions in cohesive rock by numerical modeling and laboratory experiments. *Geol. Soc. Am. Spec. Pap.* **518**, SPE518–SPE502, doi:10.1130/2015.2518(02).
- Holsapple, K. A., 1993. The scaling of impact processes in planetary sciences. *Annual Review of Earth and Planetary Sciences* **21**, 333–373.
- Holsapple, K. A., and Schmidt, R. M., 1982. On the scaling of crater dimensions: 2. Impact processes. *J. Geophys. Res.* **87**, 1849–1870, doi:10.1029/JB087iB03p01849.
- Holsapple, K. A., and Schmidt, R. M. 1987. Point source solutions and coupling parameters in cratering mechanics. *J. Geophys. Res.* **92**, 6350–6376, doi:10.1029/JB092iB07p06350.
- Housen, K. R., Schmidt, R. M., and Holsapple, K. A. 1983. Crater ejecta scaling laws: Fundamental forms based on dimensional analysis. *J. Geophys. Res.* **88**, 2485–2499, doi:10.1029/JB088iB03p02485.

- Housen, K. R. and Holsapple, K. A., 2011. Ejecta from impact craters. *Icarus* **211**, 856–875.
- Ivanov, B. A. 1983. The model of cratering in ideal-plastic media. LPS XIV, 343–344.
- Ivanov, B. A., Deniem, D., Neukum, G., 1997. Implementation of dynamic strength models into 2-D hydrocodes: Applications for atmospheric breakup and impact cratering, *Int. J. Impact Eng.* **20**, 411–430.
- Johnson, B. C., Bowling, T. J., and Melosh, H. J., 2014. Jetting during vertical impacts of spherical projectiles. *Icarus* **238**, 13–22. <http://dx.doi.org/10.1016/j.icarus.2014.05.003>.
- Johnson, B. C., Collins, G. S., Minton, D. A., Bowling, T. J., Simonson, B. M., and Zuber, M. T., 2016. Spherule layers, crater scaling laws, and the population of ancient terrestrial impactors. *Icarus* **271**, 350–359.
- Kenkmann, T., Wünnemann, K., Deutsch, A., Poelchau, M. H., Schäfer, F., and Thoma, K. 2011. Impacts cratering in sandstone: The MEMIN pilot study on the effect of pore water. *Meteorit. Planet. Sci.* **46**, 890–902, doi:10.1111/j.1945-5100.2011.01200.x.
- Kraus, R. G., Senft, L. E., and Stewart, S. T., 2011. Impacts onto H₂O ice: Scaling laws for melting, vaporization, excavation, and final crater size. *Icarus* **214**, 724–738.
- Kurosawa, K., 2015. Impact-driven planetary desiccation: The origin of the dry Venus. *Earth and Planetary Science Letters* **429**, 181–190.

- Kurosawa, K., Nagaoka, Y., Senshu, H., Wada, K., Hasegawa, S., Sugita, S., and Matsui, T., 2015. Dynamics of hypervelocity jetting during oblique impacts of spherical projectiles investigated via ultrafast imaging. *Journal of Geophysical Research: Planets* **120**, doi:10.1002/2014JE004730.
- Kurosawa, K., Okamoto, T. and Genda, H., 2018. Hydrocode modeling of the spallation process during hypervelocity impacts: Implications for the ejection of Martian meteorites. *Icarus* **301**, 219–234, doi.org/10.1016/j.icarus.2017.09.015.
- Lundborg, N., 1968. Strength of rock-like materials. *International Journal of Rock Mechanics and Mining Sciences* **5**, 427–454. [https://doi.org/10.1016/0148-9062\(68\)90046-6](https://doi.org/10.1016/0148-9062(68)90046-6).
- Maxwell, D. E., 1977. Simple Z model of cratering, ejection, and the overturned flap, in Roddy, D. J., Pepin, R. O., and Merrill, R. B. (Eds.), *Impact and Explosion Cratering*, Pergamon Press, New York, pp. 1003–1008.
- Melosh, H. J., 1984. Impact ejection, spallation, and the origin of meteorites. *Icarus* **59**, 234–260.
- Melosh, H. J., 1985. Impact cratering mechanics: Relationship between the shock wave and excavation flow. *Icarus* **62**, 339–343.
- Melosh, H. J., 1989. *Impact cratering: A geologic process*, Oxford University Press, New York.
- Melosh, H. J. and Sonett, C. P., 1986. When worlds collide: Jetted vapor plumes and the Moon’s origin, in *Origin of the Moon*. edited by Hartmann,

- W. K., Phillips, R. J., and Taylor, G. J., pp. 621–642, Lunar and Planetary Inst., Houston, Tex.
- Mitani, N. K., 2003. Numerical simulations of shock attenuation in solids and reevaluation of scaling law. *Journal of Geophysical Research* **108**, E15003.
- Mizutani, H., Kawakami, S., Takagi, Y., Kato, M., and Kumazawa, M., 1983. Cratering experiments in sands and a trial for general scaling law. *Journal of Geophysical Research* **88**, Supplement, A835–A845.
- Mizutani, H., Takagi, Y., and Kawakami, S., 1990. New scaling laws on impact fragmentation. *Icarus* **87**, 307–326.
- Nagaki, K., Kadono, T., Sakaiya, T., Kondo, T., Kurosawa, K., Hironaka, Y., Shigemori, K., and Arakawa, M., 2016. Recovery of entire shocked samples in a range of pressure from ~ 100 GPa to Hugoniot elastic limit. *Meteoritics and Planetary Science* **51**, 1153–1162.
- Neukum, G. and Ivanov, B. A. 1994. Crater size distributions and impact probabilities on Earth from lunar, terrestrial-planet, and asteroid cratering data. In: *Hazard due to comets and asteroids* Ed. Gehrels, T. pp. 359–416, T. University of Arizona Press, Tucson.
- O’Keefe, J. D., and Ahrens, T. J., 1981. Impact cratering: The effect of crustal strength and planetary gravity. *Reviews of Geophysics and Space Physics* **19**, 1–12.
- O’Keefe, J. D., and Ahrens, T. J., 1993. Planetary cratering mechanics. *J. Geophys. Res.*, **98**(E9), 17011–17028, doi:10.1029/93JE01330.

- Perret, W. R., and Bass, R. C. 1975. Free-field ground motion induced by underground explosions. Sandia report SAND74-0252.
- Pierazzo, E., Vickery, A. M., and Melosh, H. J., 1997. A reevaluation of impact melt production. *Icarus*, **127**, 408–423.
- Prieur, N. C., Rolf, T., Luther, R., Wünnemann, K., Xiao, Z., and Werner, S. C., 2017. The effect of target properties on transient crater scaling for simple craters. *J. Geophys. Res. Planets*, **122**, 1704–1726, doi:10.1002/2017JE005283.
- Richardson, J. E., Melosh, H. J., Lisse, C. M., and Carcich, B. 2007. A ballistics analysis of the Deep Impact ejecta plume: Determining comet Tempel 1's gravity, mass, density. *Icarus* **190** 357–390.
- Robbins, S. J., 2014. New crater calibrations for the lunar crater-age chronology. *Earth and Planetary Science Letters* **403**, 188–198.
- Ryder, G., 2002. Mass flux in the ancient Earth-Moon system and benign implications for the origin of life on Earth. *Journal of Geophysical Research*, **107**, 5022, doi:10.1029/2001JE001583.
- Schmidt, R. M., 1980. Meteor crater: Energy of formation Implications of centrifuge scaling. 2099–2128, paper presented at 11th Lunar and Planetary Science Conference Proceedings.
- Schmidt, R. M. and Housen K. R., 1987. Some recent advances in the scaling of impact and explosion cratering. *International Journal of Impact Engineering* **5**, 543–560.

- Stewart, S. T. and Valiant, G. J., 2006. Martian subsurface properties and crater formation processes inferred from fresh impact crater geometries. *Meteoritics and Planetary Science*, **41**, 1509–1537.
- Suzuki, A. I. and 21 coauthors, 2012. Laboratory experiments on crater scaling-law for sedimentary rocks in the strength regime. *J. Geophys. Res.* **117**, E08012, doi:10.1029/2012JE004064.
- Tillotson, J. H. 1962. Metallic equations of state for hypervelocity impact. Technical Report GA-3216, General Atomic Report.
- Vickery, A. M., 1993. The Theory of Jetting: Application to the Origin of Tektites, *Icarus* **105**, 441–453.
- Wada, K., Senshu, H., and Matsui, T., 2006. Numerical simulation of impact cratering on granular material. *Icarus* **180**, 528–545.
- Wünnemann, K., Collins, G. S., and Melosh, H. J., 2006. A strain-based porosity model for use in hydrocode simulations of impacts and implications for transient crater growth in porous targets. *Icarus* **180**, 514–527, doi:10.1016/j.icarus.2005.10.013.
- Wünnemann, K., Collins, G. S., and Osinski, G. R., 2008. Numerical modelling of impact melt production in porous rocks. *Earth and Planetary Science Letters*, **269**, 530–539.
- Wünnemann, K., Nowka, D., Collins, G. S., Elbeshausen, D., and Bierhaus, M., 2011. Scaling of impact crater formation on planetary surfaces: Insights from numerical modeling. in *Proceedings of the 11th Hypervelocity Impact Symposium*, Freiburg.

- Wünnemann, K., Zhu, M. H., and Stöffler, D., 2016. Impacts into quartz sand: Crater formation, shock metamorphism, and ejecta distribution in laboratory experiments and numerical models. *Meteorit. Planet. Sci.*, **51**(10), 1762–1794, doi:10.1111/maps.12710.
- Yamamoto, S., Wada, K., Okabe, N., and Matsui, T. 2006. Transient crater growth in granular targets: An experimental study of low velocity impacts into glass sphere targets. *Icarus* **183**, 215–224, doi:10.1016/j.icarus.2006.02.002.
- Yamamoto, S., Barnouin-Jha, O. S., Toriumi, T., Sugita, S., and Matsui, T., 2009. An empirical model for transient crater growth in granular targets based on direct observations. *Icarus* **203**, 310–319, doi:10.1016/j.icarus.2009.04.019.
- Yamamoto, S., Hasegawa, S., Suzuki, A. I., and Matsunaga, T., 2017. Impact velocity dependence of transient cratering growth. *Journal of Geophysical Research: Planets* **122**, doi:10.1002/2016JE005252.